

Tetragonal-cubic phase transition in KGaSi₂O₆ synthetic leucite analogue and its probable mechanism

BELL, Anthony <<http://orcid.org/0000-0001-5038-5621>> and HENDERSON, CMB

Available from Sheffield Hallam University Research Archive (SHURA) at:

<https://shura.shu.ac.uk/25738/>

This document is the Accepted Version [AM]

Citation:

BELL, Anthony and HENDERSON, CMB (2019). Tetragonal-cubic phase transition in KGaSi₂O₆ synthetic leucite analogue and its probable mechanism. *Journal of Solid State Chemistry*, 284, p. 121142. [Article]

Copyright and re-use policy

See <http://shura.shu.ac.uk/information.html>

Tetragonal-cubic phase transition in KGaSi₂O₆ synthetic leucite analogue and its probable mechanism.

A.M.T.Bell¹, Materials and Engineering Research Institute, Sheffield Hallam University, Sheffield, S1 1WB, UK and C.M.B.Henderson, School of Earth and Environmental Sciences, University of Manchester, Manchester, M13 9PL, UK

¹ Corresponding author, email Anthony.Bell@shu.ac.uk

Abstract. Synthetic leucite KGaSi₂O₆ at 298K is *I*4₁/*a* tetragonal and is isostructural with natural leucite (KAlSi₂O₆); with unit cell parameters of $a = 13.1099(4)$, $c = 13.8100(4)$ Å, $V = 2373.50(12)$ Å³. With increasing temperature it undergoes a reversible, displacive phase transition from *I*4₁/*a* to cubic *Ia* $\bar{3}$ *d*; this well-studied phase transition in KAlSi₂O₆ occurs at ~930K. However for KGaSi₂O₆ it is smeared out from 673 to ~970K where it consists of a mixture of the low- and high-temperature polymorphs. The proportion of the cubic phase increases with temperature; the cubic phase volume is ~ 1% larger than the coexisting tetragonal polymorph. At a fixed temperature within this 'region of coexistence' phase proportions do not change. Such features are characteristic of 1st order, diffusionless, strain-mediated, martensitic-type phase transitions. It seems that the phase transition for synthetic KGaSi₂O₆ is close to being purely ferroelastic in character.

Keywords. Phase transitions. Rietveld method. Leucite minerals. X-ray powder diffraction.

1. Introduction

1.1. Leucite crystal structures

The crystal structure of leucite, ideally KAlSi_2O_6 , consists of a three-dimensional tetrahedrally coordinated silicate framework in which one third of the tetrahedral sites (T-sites) have Al replacing Si. There are two types of channel in this framework structure; the larger (W) channels are occupied by extra-framework K^+ cations, whereas the smaller (S) channels are vacant. The framework is made up of linked four-membered and six-membered rings of TO_4 tetrahedra. At room temperature the space group of natural leucite is $I4_1/a$ tetragonal (Mazzi et al., 1976) [1]. The topologically identical crystal structure of pollucite ($\text{CsAlSi}_2\text{O}_6$), the Cs analogue of leucite, is $Ia\bar{3}d$ cubic (Beger, 1969; Yanase et al., 1997) [2, 3] with Cs^+ cations occupying the W channels and the S channels being vacant. Leucites containing extra-framework Cs cations are of technological interest as potential storage materials for Cs radioisotopes in nuclear waste [4-8]. It is also possible to have topologically equivalent leucite structures where one sixth of the tetrahedral sites is occupied by *divalent* cations; such synthetic analogues have a general formula $A_2X^{2+}\text{Si}_5\text{O}_{12}$, in which A is a monovalent alkali metal cation (K, Rb, Cs) and X is a divalent cation (Be, Mg, Mn, Fe^{2+} , Co, Ni, Zn, Cd, Cu) [9-15]; compare this to the general formula for leucite and pollucite and many synthetic analogues, $AY^{3+}\text{Si}_2\text{O}_6$, in which Y is a trivalent cation (Al, B, Fe^{3+}) [e.g., 1, 12, 16-18]. All of these crystal structures have either $Ia\bar{3}d$ or $I4_1/a$ space groups with *disordered* framework T-sites.

We have used laboratory X-ray, high-resolution synchrotron X-ray and neutron powder diffraction, together with electron diffraction and magic-angle spinning NMR to determine and refine $A_2X^{2+}\text{Si}_5\text{O}_{12}$ $P2_1/c$ monoclinic (Bell et al., 1994a; Bell and Henderson, 2018) ($A = \text{K}$, $X = \text{Mg}$, Fe, Co, Zn) [14,19] and $Pbca$ orthorhombic ($A = \text{Rb}$, Cs, $X = \text{Mg}$, Mn, Co, Ni, Cu, Zn, Cd) leucite-type crystal structures in which the framework T-site cations are *ordered* (Bell et al., 1994b; Bell and Henderson, 1996, 2009, 2016; Bell et al., 2010) [15, 20-23].

1.2. Leucite structure phase transitions.

Phase transitions from $I4_1/a$ (point group $4/m$) tetragonal to $Ia\bar{3}d$ (point group $m\bar{3}m$) cubic structures (e.g., Peacor, 1968; Taylor and Henderson, 1968; Dove et al., 1993; Ito et al., 1995; Palmer et al., 1997) [24-28] have been observed as the temperature increases in natural leucite and leucite analogues. Note that an intermediate tetragonal phase in this transition ($I4_1/acd$, point group $4/mmm$) has been reported (Lange et al., 1986; Palmer et al., 1990; Heaney and Veblen, 1990) [29-32]. This phase transition in KAlSi_2O_6 leucite is displacive, rapid, reversible and continuous (Taylor and Henderson, 1968; Palmer et al., 1997; Lange et al., 1986; Palmer et al., 1989; Wyart, 1937; Faust, 1963; Carpenter et al., 1998) [25, 28-30, 33-35]. A distinctive optical feature of tetragonal natural leucite is its multiple lamellar twinning (pseudomerohedral twins)

together with cross-cutting multiple merohedral twins [32, 36]; the former is present as a result of the $m\bar{3}m$ to $4/m\bar{m}m$ transition and the latter from $4/m\bar{m}m$ to $4/m$. Note that the high-temperature cubic polymorph is untwinned and the transformation twinning commonly forms lamellae of width ~ 100 - 300 nm. In high-temperature XRD and TEM studies, when cycling across this phase transition, the leucite shows a well-known ‘memory’ effect where, below the transition, twinning reappears in much the same overall proportions as in the original crystal with closely similar twin boundary positions [1, 24, 32, 36].

A phase transition from $I\bar{4}3d$ cubic to $Ia\bar{3}d$ cubic has also been reported in the synthetic boron-bearing leucite KBSi_2O_6 on heating [17]. In all of these transitions T-site cation disorder is retained. A phase transition from $P2_1/c$ monoclinic to $Pbca$ orthorhombic (Redfern and Henderson, 1996) [37] has also been observed on heating hydrothermally synthesized $\text{K}_2\text{MgSi}_5\text{O}_{12}$; in this transition, T-site cation order is retained. A high temperature synchrotron X-ray powder diffraction study on $\text{Cs}_2\text{ZnSi}_5\text{O}_{12}$ (Bell and Henderson, 2012) [38] showed a reversible phase transition from $Pbca$ orthorhombic to $Pa\bar{3}$ cubic, this was the first reported leucite phase transition showing a change from ordered to disordered T-site cations. Two phase transitions have been reported in high pressure single-crystal X-ray studies of leucite-type structures (Gatta et al., 2008, 2009b) [39, 40]; natural leucite, KAlSi_2O_6 , undergoes a phase transition from $I4_1/a$ tetragonal to $P1$ triclinic at 2.4 (2) GPa; pollucite, $(\text{Cs,Na})_{16}\text{Al}_{16}\text{Si}_{32}\text{O}_{96}\cdot n\text{H}_2\text{O}$, undergoes a phase transition from $Ia\bar{3}d$ cubic to $P1$ triclinic at 0.66(12) GPa. The unit-cell parameters have been reported for these triclinic structures, but no other structural parameters are known.

Henderson et al. (2017) [18] recently pointed out that the multiplicity of Space Groups shown by phases having a leucite-type structure (including $I4_1/a$, $I4_1/acd$, $I\bar{4}3d$, $Pa\bar{3}$, $Pbca$, $P2_1/c$) are all isotropy subgroups of the $Ia\bar{3}d$ aristotype and Knight and Henderson (2019) [41] determined a universal aristotype crystal structure for such phases by using a non-linear optimisation of the fractional coordinates.

1.3. Gallium containing leucite analogues.

Leucite analogues with trivalent framework cations ($AY^{3+}\text{Si}_2\text{O}_6$) are known for $Y = \text{Ga}$ with $A = \text{K}$, Rb and Cs . These are present as patterns in the Powder Diffraction File [42]; KGaSi_2O_6 [PDF pattern 37-349] and $\text{RbGaSi}_2\text{O}_6$ [PDF pattern 37-350] are both $I4_1/a$ tetragonal and are isostructural with natural leucite.

$\text{CsGaSi}_2\text{O}_6$ [PDF pattern 50-175] is $I\bar{4}3d$ cubic. However, no other structural information is known for these gallium containing leucites. There is a published single-crystal structure of $\text{K}_{0.8}\text{Rb}_{0.2}\text{GaSi}_2\text{O}_6$ (Klaska, 1978) [43], this is $I4_1/a$ tetragonal and this structure shows partial T-site cation ordering.

2. Experimental methods.

2.1 Synthesis

KGaSi₂O₆ was prepared from a stoichiometric mixture of K₂CO₃, Ga₂O₃ and SiO₂. The mixture was initially heated at 1673 K in an Elite BRF16/10 furnace for 3 hours as described in Powder Pattern 37-349. The resultant material was then reground using a Retsch RS200 mill with steel grinding discs and heated at 1273K for 4 days; this produced a white crystalline powder.

2.2. Ambient temperature X-ray powder diffraction

The white powder was mounted on a low-background silicon wafer prior to ambient temperature X-ray powder diffraction. Data (10 – 100 °2θ) were collected with a PANalytical X'Pert Pro MPD using Cu K_α radiation, a Ni β filter, and an X'Celerator area detector.

2.3 High temperature X-ray powder diffraction

The sample was loaded on a Pt flat plate sample holder in an Anton-Paar HTK1200N high temperature stage which was mounted on the X'Pert. XRD data were collected over the range 24.5-28.0 °2θ; this showed the tetragonal (004) and (400) Bragg reflections for KGaSi₂O₆. XRD data were collected at 298K, 373-673K (100K steps) 698-948K (25K steps) and 973-1273K (100K) steps. On heating, a third Bragg reflection appears at about 673K between the two tetragonal peaks, this is due to the $Ia\bar{3}d$ cubic (400) Bragg reflection. On further heating this (400) peak gets stronger and the two tetragonal peaks move together, get weaker and are not present at 973K (see Figure 1). Longer duration scans were then obtained over the range 10-80°2θ at 298K, and then 373 to 1073K (100K steps); a further scan was also done at 1473K. A final scan was done when the sample had cooled to room temperature to establish that the high-temperature cubic phase had fully transformed back to the tetragonal phase.

2.4. Scanning electron microscopy

KGaSi₂O₆ powder was mounted on a carbon sticky tab on an aluminium sample holder; gold coated and scanned using a FEI Quanta 650 SEM. The crushed powder consists of clusters of birefringent grains of various sizes; an SEM image of the sample (Figure 2) shows that the largest grains are ~ 25 μm with sizes ranging down to ~200 nm.

2.5 Thermal analysis

A Netsch Proteus Thermal Analyser was used to collect Differential Thermal Analysis (DTA) data on a sample of KGaSi₂O₆ powder. 0.1004g of powder was loaded into an Al₂O₃ sample cup, the sample was heated at 20K/minute between 306-1144K, the data collection time was 43 minutes. From the temperature difference between KGaSi₂O₆ powder and an empty Al₂O₃ sample cup a DTA trace (Figure 3) was plotted.

2.6 Data analysis

2.6.1. Ambient temperature

The ambient temperature XRD data matched the Powder Diffraction File pattern for KGaSi_2O_6 . Rietveld refinements [44] were done using FULLPROF [45]. The starting model for Rietveld refinements was taken from the $I4_1/a$ tetragonal structure of leucite KAlSi_2O_6 [1] with Ga replacing Al on the T-sites. T-O distances were constrained to 1.68(2) Å (average bond distance for tetrahedral Si-O and Ga-O) assuming complete T-site disorder (1/3Ga:2/3Si on each T-site) as it was not possible to refine chemically sensible T-site occupancies. KGaSiO_4 [46] was included as a second phase. The strategy for Rietveld refinement had the parameters refined in the following order:- scale factors, zeropoint and lattice parameters, background parameters and profile parameters. After this atomic coordinates and U_{iso} temperature parameters for the KGaSi_2O_6 phase were refined, no atomic coordinates and U_{iso} parameters were refined for the KGaSiO_4 second phase. The U_{iso} parameters for Si and Ga on each T-site were constrained to be the same although the U_{iso} parameters for Si and Ga were different for different T-sites. The U_{iso} parameters for the six O atom sites were constrained to have the same value. Rietveld refinement showed that the KGaSiO_4 second phase was present at 3.0(2) wt.%. Figure 4 shows the two-phase Rietveld difference plot for ambient temperature KGaSi_2O_6 . Table 1 shows the refined structural parameters for this ambient temperature dataset. R_p , R_{wp} , R_{exp} and χ^2 parameters from the Rietveld refinement are also included. Table 2 shows the K-O and T-O refined interatomic distances for $I4_1/a$ tetragonal KGaSi_2O_6 and Table 3 shows the O-T-O and T-O-T interatomic angles for $I4_1/a$ tetragonal KGaSi_2O_6 .

atom	x	y	z	$U_{\text{iso}} (\text{\AA}^2)$	occupancy
K1	0.3733(12)	0.3715(11)	0.1125(14)	0.175(6)	1.0000
Ga1	0.0529(6)	0.3884(7)	0.1685(7)	0.053(5)	0.3333
Ga2	0.1641(8)	0.6128(7)	0.1212(8)	0.074(4)	0.3333
Ga3	0.3894(8)	0.6413(7)	0.0846(6)	0.091(5)	0.3333
Si1	0.0529(6)	0.3884(7)	0.1685(7)	0.053(5)	0.6667
Si2	0.1641(8)	0.6128(7)	0.1212(8)	0.074(4)	0.6667
Si3	0.3894(8)	0.6413(7)	0.0846(6)	0.091(5)	0.6667
O1	0.1124(17)	0.3171(18)	0.0902(18)	0.086(6)	1.0000
O2	0.103(2)	0.4965(16)	0.1343(16)	0.086(6)	1.0000
O3	0.1688(17)	0.6613(11)	0.231(11)	0.086(6)	1.0000
O4	0.147(2)	0.6893(11)	0.0327(11)	0.086(6)	1.0000
O5	0.2902(11)	0.5779(17)	0.136(2)	0.086(6)	1.0000
O6	0.4900(12)	0.6045(15)	0.1398(18)	0.086(6)	1.0000

KGaSi_2O_6 $I4_1/a$ tetragonal - 97(2) weight%

$$a(\text{\AA}) = 13.1099(4)$$

$$c(\text{\AA}) = 13.8100(4)$$

$$V(\text{\AA}^3) = 2373.50(12)$$

KGaSiO_4 $P6_3$ hexagonal - 3.0(2) weight%

$$a(\text{\AA}) = 18.174(3)$$

$$c(\text{\AA}) = 8.5270(19)$$

$$V(\text{\AA}^3) = 2439.0(8)$$

$$R_p = 1.6034, R_{\text{wp}} = 2.3394, R_{\text{exp}} = 0.8871, \chi^2 = 6.954$$

Table 1. Refined atomic coordinates, temperature factors (U_{iso}) and lattice parameters for $I4_1/a$ tetragonal KGaSi_2O_6 . All atoms are on the $16f$ general position for $I4_1/a$, Si and Ga are disordered over the same sites. Lattice parameters for KGaSiO_4 impurity phase are also given. Data from ambient temperature dataset collected outside the furnace.

atom 1	atom 2	distance (Å)	atom 1	atom 2	distance (Å)
K1	O1	3.51(3)	T1	O1	1.63(2)
K1	O1	3.24(3)	T1	O1	1.61(2)
K1	O2	3.92(3)	T1	O2	1.63(2)
K1	O2	3.38(3)	T1	O4	1.58(2)
K1	O3	3.33(3)	T2	O2	1.73(2)
K1	O3	3.17(3)	T2	O3	1.65(2)
K1	O4	2.87(3)	T2	O4	1.60(2)
K1	O4	3.90(3)	T2	O5	1.73(2)
K1	O5	2.93(3)	T3	O3	1.66(2)
K1	O5	3.39(3)	T3	O5	1.70(2)
K1	O6	3.44(2)	T3	O6	1.60(2)
K1	O6	3.41(3)	T3	O6	1.66(2)
mean K-O		3.37(3)	mean T-O		1.65(2)

Table 2. Refined K-O and T-O distances (T = disordered Si and Ga) for $I4_1/a$ tetragonal KGaSi_2O_6 . Data from ambient temperature dataset collected outside the high temperature stage.

atom 1	atom 2	atom 3	angle
O1	T1	O1	107(2)
O1	T1	O2	97(2)
O1	T1	O4	132(2)
O1	T1	O2	124(2)
O1	T1	O4	99(2)
O2	T1	O4	102(2)
mean O-T1-O			110(2)
O2	T2	O3	105(2)
O2	T2	O4	125(2)
O2	T2	O5	101(2)
O3	T2	O4	118(2)
O3	T2	O5	88(2)
O4	T2	O5	113(2)
mean O-T2-O			108(2)
O3	T3	O5	105(2)
O3	T3	O6	97(2)
O3	T3	O6	133(2)
O5	T3	O6	107(2)
O5	T3	O6	99(2)
O6	T3	O6	114(2)
mean O-T3-O			109(2)
mean O-T-O			109(2)
T1	O1	T1	135(1)
T1	O2	T2	169(1)
T2	O3	T3	135(1)
T1	O4	T2	144(1)
T2	O5	T3	124(1)
T3	O6	T3	142(1)
mean T-O-T			142(1)

Table 3. Refined intratetrahedral O-T-O and intertetrahedral T-O-T (T = disordered Si and Ga) angles (in degrees) for $I4_1/a$ tetragonal KGaSi_2O_6 . Data from ambient temperature dataset collected outside the high temperature stage.

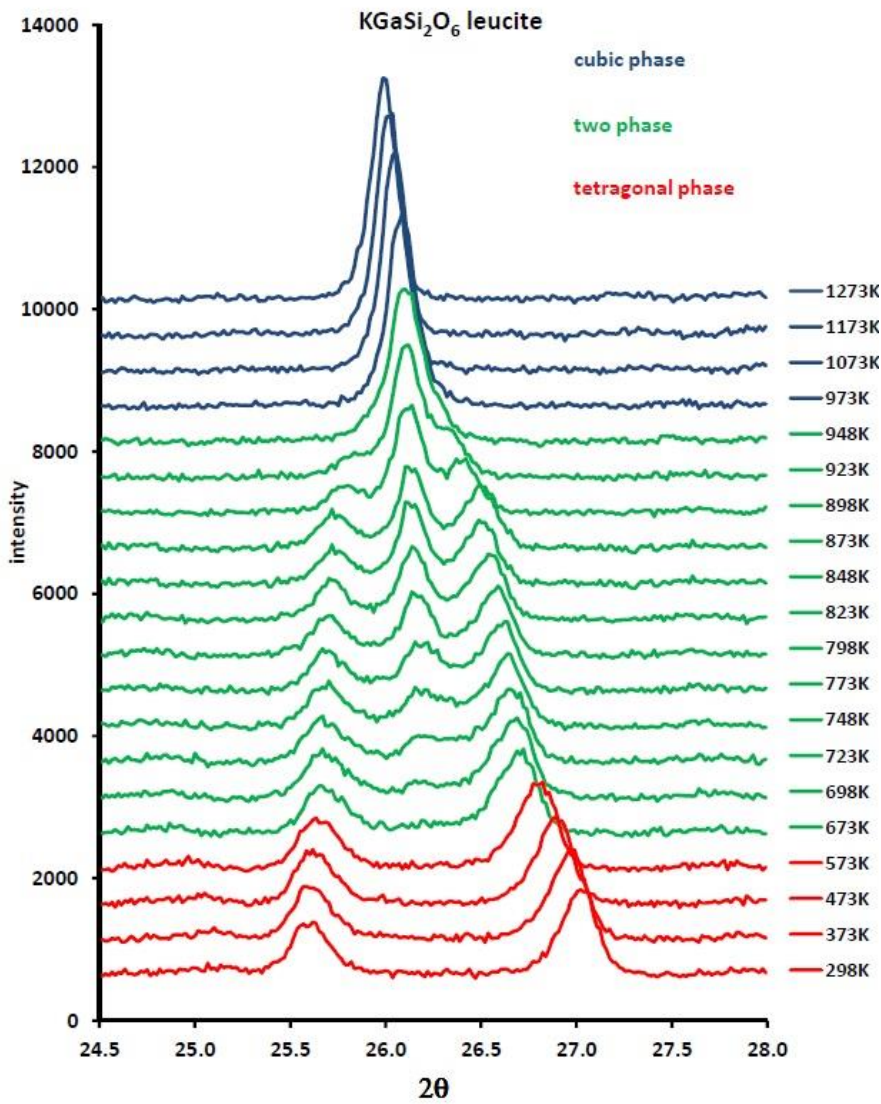


Figure 1. Plot showing XRD data for KGaSi₂O₆ 24.5-28.0°2θ over the temperature range 298-1273K. This shows how the two tetragonal (004) and (400) Bragg reflections for KGaSi₂O₆ are joined by a third cubic (400) Bragg reflection in the two phase region. Only the cubic (400) Bragg reflection remains in the cubic phase region. COLOUR FIGURE.

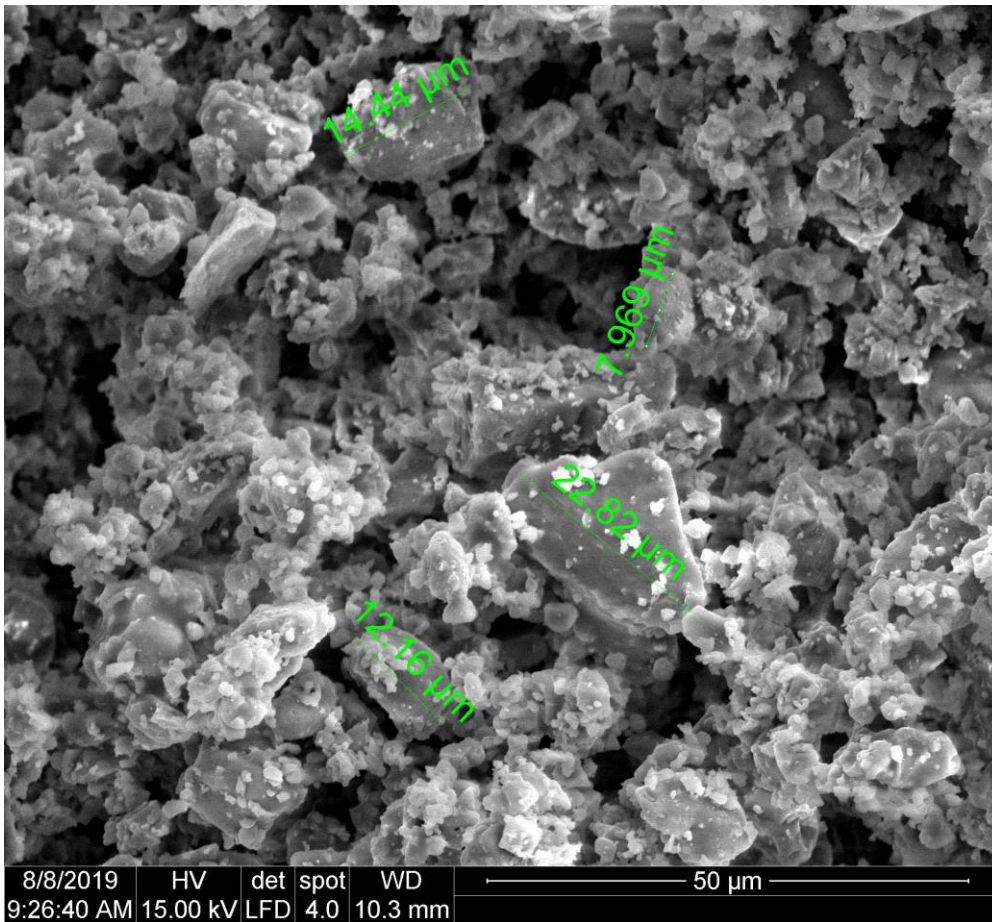


Figure 2. SEM image of the powder sample used to study the tetragonal to cubic phase transition in KGaSi_2O_6 with high-temperature PXRD. The largest grains are ~ 25 microns but these are mixed with powder particles down to about 200nm. COLOUR FIGURE.

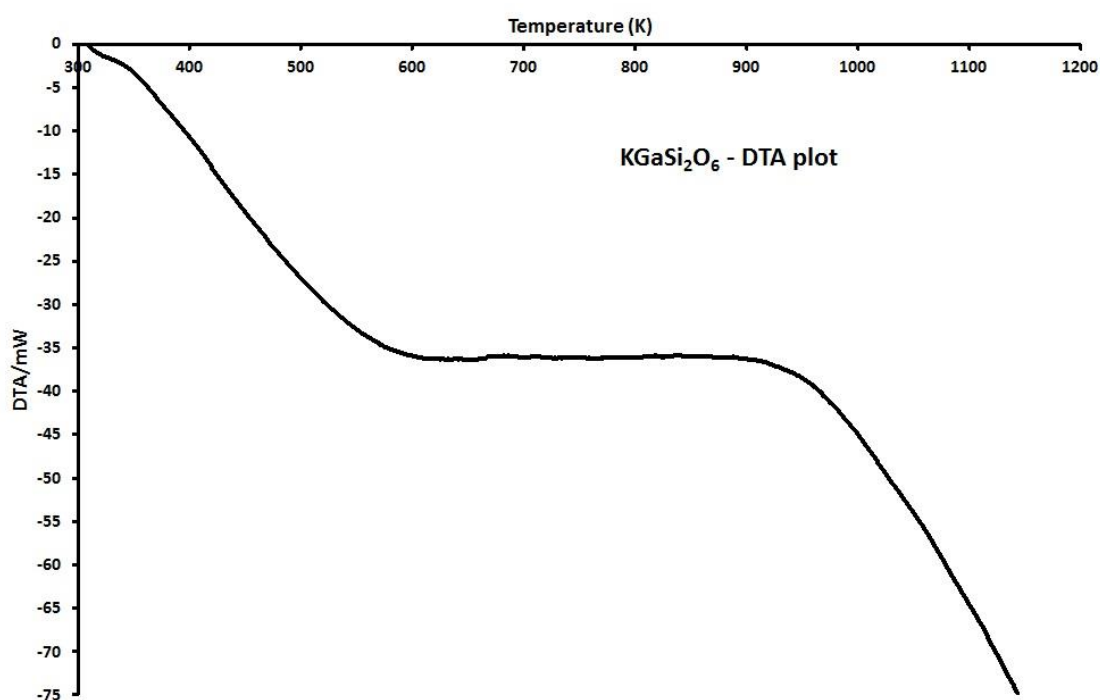


Figure 3. Differential Thermal Analysis plot for KGaSi_2O_6 306-1144 K.

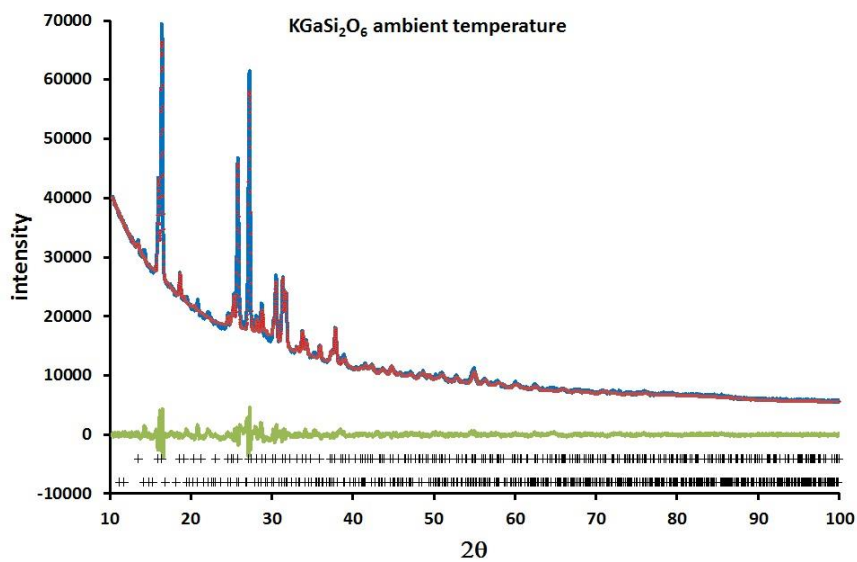


Figure 4. Two-phase Rietveld difference plot for KGaSi_2O_6 sample at ambient temperature. Red dots show observed XRD data, blue line shows calculated XRD data and green line shows the difference between observed and calculated. Upper and lower crosses respectively show positions of Bragg reflections for the KGaSi_2O_6 phase and the impurity KGaSiO_4 phase. COLOUR FIGURE.

The mean K-O distance of 3.37(3) Å for the 12 nearest neighbour oxygens (NNO) is significantly larger than the Shannon (1976)[47] K-O₁₂ distance (3.02 Å) and this is also true for the mean distance to the six nearest oxygens in our sample of KGaSi₂O₆ (i.e. mean K-O₆ = 3.15(3) Å). Such ‘long’ K-O distances are a consistent feature of single crystal and powder structural determinations reported for natural KAl-leucite and Gatta et al. (2008) [39] predicted that the theoretical coordination number for K in natural leucite is 9 at 1 bar while Mazzi et al. [1] commented that the distances to the outer set of 6 oxygens range from 3.5 to 3.8 Å and that such distances are too long to be considered as bond distances. Thus it is clear that the K atoms in these leucites are underbonded to the nearest neighbour oxygen anions; this seems to be true irrespective of the size of the alkali cavity cations (K-Cs) occupying the large cavity site (e.g., Henderson et al., 2017 [18]). Indeed, it may be generally the case that the sizes of the large channels in disordered leucite frameworks reflect the intrinsic properties of the framework, rather than being controlled by its collapse about the cavity cations present, as has been suggested by Henderson et al. (2017) [18] for disordered $Ia\bar{3}d$ K₂X²⁺Si₅O₁₂ leucites (see also Knight and Henderson, 2019) [41].

2.6.2. High temperature.

Single-phase $I4_1/a$ tetragonal refinements (FULLPROF) for KGaSi₂O₆ were done at 298-573K and single-phase $Ia\bar{3}d$ cubic refinements were done at 973K, 1073K and 1473K. As the high temperature scans were done with a smaller sample holder and shorter scan times than the ambient temperature scan done outside the high temperature stage it was not possible to detect the presence of KGaSiO₄ impurity phase, the high temperature data are quite noisy compared to the ambient temperature data measured outside the Anton-Paar HTK1200N high temperature stage. The $Ia\bar{3}d$ cubic structure of pollucite CsAlSi₂O₆ [2], with Ga replacing Al and K replacing Cs, was used as a starting model for the cubic phase. The strategy for Rietveld refinement for the data collected in the high temperature stage had the parameters refined in the following order:- scale factors, zeropoint and lattice parameters, background parameters and profile parameters. For the $I4_1/a$ KGaSi₂O₆ phase the U_{iso} parameters for Si and Ga on each T-site were constrained to be the same although the U_{iso} parameters for Si and Ga were different for different T-sites, the U_{iso} parameters for the six O atom sites were constrained to have the same value. For the $Ia\bar{3}d$ KGaSi₂O₆ phase the structure has only one K site, one T-site (with disordered Si and Ga) and one O site, as in the $I4_1/a$ KGaSi₂O₆ phase the U_{iso} parameters for Si and Ga on the T-site were constrained to be the same. In the two-phase region the refinement of with the 873K data had the O atom U_{iso} parameters for the $I4_1/a$ KGaSi₂O₆ phase fixed at zero as they could not be refined to chemically sensible positive values. In the two-phase region the refinement of with the 773K data all parameters for both the $I4_1/a$ and $Ia\bar{3}d$ KGaSi₂O₆ phases could be refined. In the two-phase region the refinement of with the 673K data the atomic coordinates, U_{iso} parameters and profile parameters for the $Ia\bar{3}d$ KGaSi₂O₆ phase were fixed at the values from the refinement of with the 773K data

as they could not be refined to chemically sensible positive values. The same T-O distance constraints were applied to all of the $I4_1/a$ tetragonal refinements for high temperatures as were applied for the ambient temperature refinement. Figure 5 shows the two-phase Rietveld difference plot for KGaSi_2O_6 obtained at 873K. Two-phase Rietveld refinements were done over the range 673-873K, where $I4_1/a$ tetragonal KGaSi_2O_6 is phase 1 and $Ia\bar{3}d$ cubic KGaSi_2O_6 is phase 2. The refined high-temperature data provides reliable unit cell parameters and phase proportions but the fits are not considered to be reliable enough to report low-error atomic coordinates, bond distances and bond angles.

2.7. Additional ambient temperature X-ray powder diffraction

XRD data were also collected on two powdered leucite (KAlSi_2O_6) samples; these are synthetic sample HL.26 and natural leucite 28054. Both samples were mounted on low-background silicon wafers prior to ambient temperature X-ray powder diffraction. Data ($5 - 100^\circ 2\theta$) were collected with a PANalytical X'Pert Pro MPD using Cu K_α radiation, a Ni β filter, and a PIXCEL-1D area detector.

2.8. Crystallite size estimation for leucite samples.

Crystallite sizes for KGaSi_2O_6 and the leucite (KAlSi_2O_6) samples HL.26 and 28054 were estimated from the Full Width Half Maximum (FWHM) of the tetragonal (004) and (400) leucite Bragg reflections for each sample.

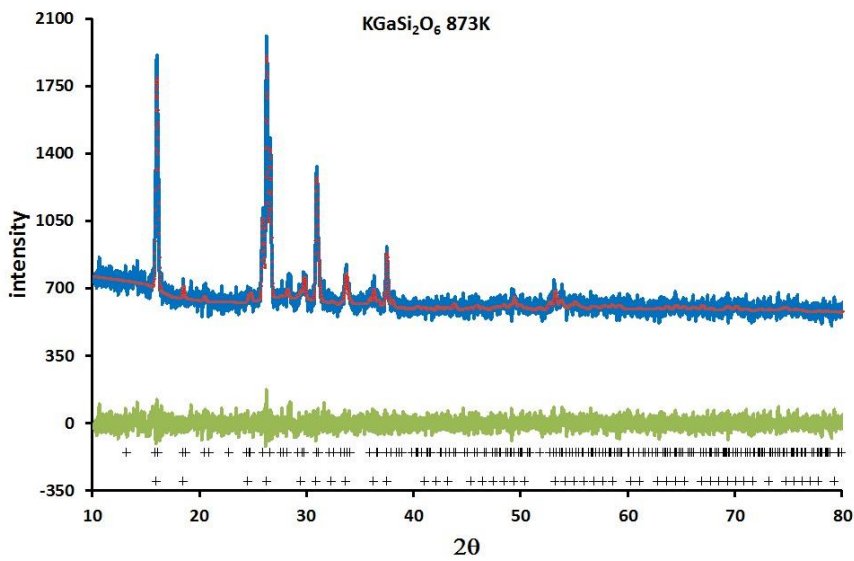


Figure 5. Two-phase Rietveld difference plot for KGaSi₂O₆ sample at 873K. Red dots show observed XRD data, blue line shows calculated XRD data and green line shows the difference between observed and calculated. Upper and lower crosses respectively show positions of Bragg reflections for the $I4_1/a$ tetragonal KGaSi₂O₆ phase and the $Ia\bar{3}d$ cubic KGaSi₂O₆ phase. COLOUR FIGURE.

The PANalytical HighScore Plus software was used to do profile fitting on the (004) and (400) leucite and the silicon standard 111 Bragg reflections. The measured 2θ angles and FWHM for each (004) and (400) Bragg reflection were used in the Scherrer equation to determine estimates of the crystallite sizes for the (004) and (400) leucite Bragg reflections; the FWHM of the silicon 111 Bragg reflection was used to calibrate the instrumental contribution to the widths of the Bragg reflections. The estimated crystallite sizes for each leucite sample were taken from the mean of the crystallite sizes determined from the (004) and (400) reflections for each phase. These results are given in Table 4.

Sample name Starting material	KGaLc1 Glass	Nat Lc 28054 ^f	HL.26 Gel ^d	KLc 1 Gel ^d	L.60 Gel ^d	L.110 Gel ^d	Nat Lc ^h A.1776
Composition wt%	KGaSi ₂ O ₆ KGa-Lc	KLc _{0.95} NaLc _{0.05} + 0.7 wt % Fe ₂ O ₃ ^c	KAlSi ₂ O ₆ KAl-Lc	KAlSi ₂ O ₆ KAl-Lc	KLc _{0.96} Or _{0.04} ^d K _{0.99} □ _{0.01} Al _{0.99} Si _{2.01} ^c	KLc _{0.925} Or _{0.075} ^d K _{0.925} □ _{0.075} Al _{0.925} Si _{2.075} ^c	KLc _{0.88} Or _{0.12} + 2.1 wt.% Fe ₂ O ₃ ^g
Synthesis conditions	1 bar, 1273K, 4 days	Natural mineral	1 bar~1673K 1 hour	1 bar 1573K 3 days	1 kbar, 1173K 7 days	1 kbar, 1273K, 7 days	Natural mineral
Peak FWHM °2θ/ Crystallite size, nm This work	(004) 0.22/87 ^a (400) 0.21/93 ^a	(004) 0.16/402 ^a (400) 0.17/288 ^a	(004) 0.17/262 ^a (400) 0.20/138 ^a				
Average (004/400) FWHM °2θ from old charts [54] and/or average crystallite size, nm	Average size 90 ^a	Average size 345 ^a Average FWHM ~ 0.17 ^b	Average size 200 ^a Average FWHM ~ 0.20 ^b	Average FWHM/size ~0.28/136 ^b	Average FWHM/size ~0.18/210 ^b	Average FWHM/size ~0.19/200 ^b	Average FWHM/size ~0.19/200 ^b
Heating Inversion starts K	~670		810(10)	~650		750(10)	~690
Heating Inversion ends K	~970	990(5)	920(10)	890(10)	950(5)	870(10)	840(10)
Cooling Inversion starts K		980(10)	880(10)	~890	950(5)	850(10)	820(10)
Cooling Inversion ends K			720(10)	?		700(10)	~640
V _t Å ³	2465		2467	2467		2444	2419
V _c Å ³	2490		2482	2482		2468	2438
ΔV %	1.0		~0.5	~0.6		1.0	0.8
T (K)	870		870	790		800	745

^a FWHM and crystallite size this work; ^b FWHM from CMBH old X-ray charts, crystallite sized based on crystallite sizes determined for HL.26 and 28054 in this work;

^c Chemical analysis from Taylor and Henderson [25]; ^d prepared by gel method of Hamilton and Henderson [57]; ^e □ number of vacancies per formula unit; ^f hand-picked phenocryst fragments; ^g Microprobe analysis from Lange et al. [29]; ^h Heating experiments on crushed bulk rock sample due to microcrystalline sizes (< 100 μm). ⁱ cell volume data during heating; measured at temperature (T) shown. V_t = tetragonal volume, V_c = cubic volume,

KLc = leucite KAlSi₂O₆, KGa-Lc = KGaSi₂O₆, NaLc = leucite NaAlSi₂O₆ Or = orthoclase - potassium alkali feldspar KAlSi₃O₈

Table 4. Tetragonal–cubic transformation properties for synthetic and natural K-rich leucites

3. Results and discussion.

The crushed powder used for XRD study was mounted in refractive index oil and inspected with a polarising petrological microscope. The largest grains are about 20–30 μm across; these under plane polarised light were clear and with cross polarised light (CPL) were found to be birefringent due to twinning. The bulk of the powdered sample consists of poorly defined clusters of fine-grained particles which showed ‘pin-pricks’ of birefringence in CPL consistent with their tetragonal structure.

3.1. Dependence of KGaSi_2O_6 leucite structure on temperature

At ambient temperature KGaSi_2O_6 is isostructural with KAlSi_2O_6 and $\text{KFe}^{3+}\text{Si}_2\text{O}_6$; both have the T-site cation disordered $I4_1/a$ tetragonal structure. The tetragonal structure is retained on heating to 573K, however at 673K a phase transition begins and a high-temperature $Ia\bar{3}d$ cubic polymorph (isostructural with pollucite $\text{CsAlSi}_2\text{O}_6$) appears. Between 673 and 943K a two-phase region occurs. Thus, at about 673K the cubic $(004)_c$ peak appears between the tetragonal $(400)_t$ and $(004)_t$ peaks and on further heating this $(400)_c$ peak gets stronger and the two tetragonal peaks move together and get weaker (see Figure 1). Thus at 923 K the $(004)_c$ peak for the growing cubic phase shows small shoulders towards its base while only a slight broadening at its flanks is present at 943 K. It is clear that as temperature increases the peaks for the residual tetragonal phase $(400)_t$ and $(004)_t$ become weaker, move closer together steadily, and are no longer detectable at 973 K. We place the end of the phase transition at 970 ± 10 K. Figure 3 shows the DTA plot for KGaSi_2O_6 over the range 306-1144 K, this shows that the DTA curve flattens out over the approximate temperature range 600-900 K. The temperature range for this change in the DTA curve is approximately the same as the temperature range for the two-phase region observed by XRD. After cooling to ambient temperature, the structure had reverted to the $I4_1/a$ tetragonal polymorph consistent with it being a reversible displacive transition (e.g., Taylor and Henderson, 1968; Palmer et al., 1997) [25, 28].

Table 5 shows the refined unit cell parameters and phase proportions (wt. %) for KGaSi_2O_6 on heating; also shown are the unit cell parameters at room temperature after the heating cycle. R_p , R_{wp} , R_{exp} and χ^2 parameters from the Rietveld refinements are also included. With increasing temperature the a axis for the tetragonal polymorph shows a marked increase and the c axis a much smaller decrease; these are the expected changes for the leucite structure as the trend towards a more isometric phase takes place continuously (Figure 6a). The a lattice parameter for the newly formed cubic polymorph shows a steady increase for the cubic component of the mixed phase region (680 to 880K) indicating a continuous trend with the cubic single-phase region. We will refer to the two-phase stage as the ‘region of coexistence’ (*cf.* Henderson and Taylor, 1982) [48]. As expected, the c/a ratio for the $I4_1/a$ tetragonal structure decreases progressively on heating as the temperature approaches the phase transition temperature (Figure 6b).

T (K)	tetragonal phase					cubic phase			R-factors			
	a (Å)	c (Å)	V (Å ³)	c/a	% phase	a (Å)	V (Å ³)	% phase	R _p	R _{wp}	R _{exp}	χ ²
298	13.1279(11)	13.8266(12)	2382.9(3)	1.0532(2)	100				3.4656	4.3541	3.9344	1.2248
373	13.1553(11)	13.8234(12)	2392.3(3)	1.0508(2)	100				3.5366	4.4688	3.9278	1.2944
473	13.1904(10)	13.8105(11)	2402.8(3)	1.0470(2)	100				3.4386	4.3245	3.9242	1.2144
573	13.2319(11)	13.7995(13)	2416.1(4)	1.0423(2)	100				3.5567	4.4799	3.9253	1.3025
673	13.2824(12)	13.7877(13)	2432.5(4)	1.0380(2)	91(3)	13.470(3)	2444.2(8)	9.4(6)	3.4711	4.3616	3.9207	1.2375
773	13.3139(15)	13.7708(17)	2441.0(5)	1.0343(2)	65(3)	13.5104(15)	2466.1(5)	36(2)	3.4646	4.3389	3.9109	1.2308
873	13.3939(14)	13.7420(16)	2465.3(5)	1.0260(2)	51(3)	13.5541(13)	2490.1(4)	49(3)	3.4578	4.3388	3.9024	1.2361
973						13.5829(5)	2505.97(17)	100	3.6374	4.6211	3.9220	1.3883
1073						13.6028(5)	2516.99(16)	100	3.5771	4.6009	3.9171	1.3796
1473						13.6521(7)	2544.5(2)	100	5.6737	7.1475	6.4931	1.2117
*298	13.1183(14)	13.8247(14)	2379.1(5)	1.0538(2)	100				5.4387	6.8516	6.5027	1.1102

Table 5. Variation of lattice parameters and phase proportions with temperature (T) for $I4_1/a$ tetragonal and $Ia\bar{3}d$ cubic KGaSi_2O_6 phases. Data collected using HTK1200N furnace stage, * indicates a scan done at 298K on cooling after heating to 1473K.

Figure 6c shows steady increases for the cell volumes of both tetragonal and cubic phases and it is clear that the unit cell volume for the $Ia\bar{3}d$ cubic phase is larger than the volume for the corresponding $I4_1/a$ tetragonal phase in the two-phase region and, for example, at 773 K shows a positive ΔV of $\sim 1.0\%$. The volume thermal expansion coefficient of the tetragonal polymorph is smaller than that for the cubic phase, however, based mainly on the volume for the highest temperature point, we tentatively suggest a smaller expansion rate for the final expansion stage similar to that reported for synthetic KAlSi_2O_6 (Taylor & Henderson [25]). Figure 6d shows that the Rietveld fitted proportions for the coexisting phases in the region of coexistence steadily changes as temperature increases reflecting the progression of the tetragonal to cubic phase transition. Figure 7 shows VESTA [49] plots for the crystal structures of $I4_1/a$ tetragonal and $Ia\bar{3}d$ cubic KGaSi_2O_6 viewed down the [111] direction which defines the orientation of the large channel in the structure. This central channel of the leucite structure, which contains the K^+ cations, is less distorted in the cubic structure compared to the tetragonal structure reflecting the less collapsed and more symmetrical nature of the high-temperature, cubic framework. This structural feature defines the percolation channel which allows thermal diffusion of alkali (W) cations and is responsible for the high-ionic conductivity of members of the leucite/pollucite group of framework materials [50, 51].

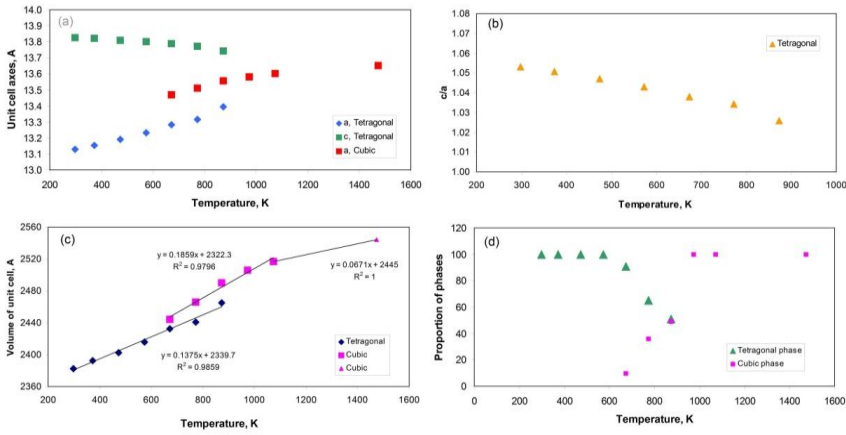


Figure 6. Unit cell parameters and phase proportions for $I4_1/a$ tetragonal and cubic $Ia\bar{3}d$ phases of KGaSi_2O_6 in the temperature range 298 to 1473 K. Figure 6a, a and c cell edges, note the occurrence of coexisting cubic and tetragonal phases at 673 – 873 K; Figure 6b, c/a unit cell ratio; Figure 6c, cell volumes including linear fits to three stages in the thermal evolution; Figure 6d, proportions of the two phases through the expansion and phase transition. COLOUR FIGURE.

3.1.1. Mechanism of the tetragonal – cubic phase transition in $I4_1/a$ leucites

The lattice parameters and phase proportions of the coexisting tetragonal and cubic phases for KGaSi_2O_6 over the temperature range defining the region of coexistence (673–873K) show important differences to the characteristics shown by the phase transition for natural KAlSi_2O_6 leucite [25, 28, 30–31]. The continuous nature of the transition for natural leucite with no volume discontinuity suggests that it is a 2nd order transition while those described here for KGaSi_2O_6 are consistent with it being a 1st order transition and it is interesting to consider how such differences might affect the spontaneous strain associated with this type of phase transformation.

Palmer et al. (1997) [28], Palmer 1990) [31] and Carpenter et al. (1998) [35] have dealt with the thermal expansion and deformation of the three-dimensional framework structure in terms of a strain ellipsoid. The strain tensor e_{ij} would have six independent components; e_{11} , e_{12} , e_{13} , e_{22} , e_{23} , e_{33} and for a cubic – tetragonal transition the strain ellipsoid has its cartesian axes coincident with the crystallographic axes which leads to $e_{12} = e_{13} = e_{23} = 0$. For such a symmetrical tensor the eigen values ϵ_1 (cf. e_{11}), ϵ_2 (cf. e_{22}), ϵ_3 (cf. e_{33}) are the tensile strains for the principal axes of the strain ellipsoid.

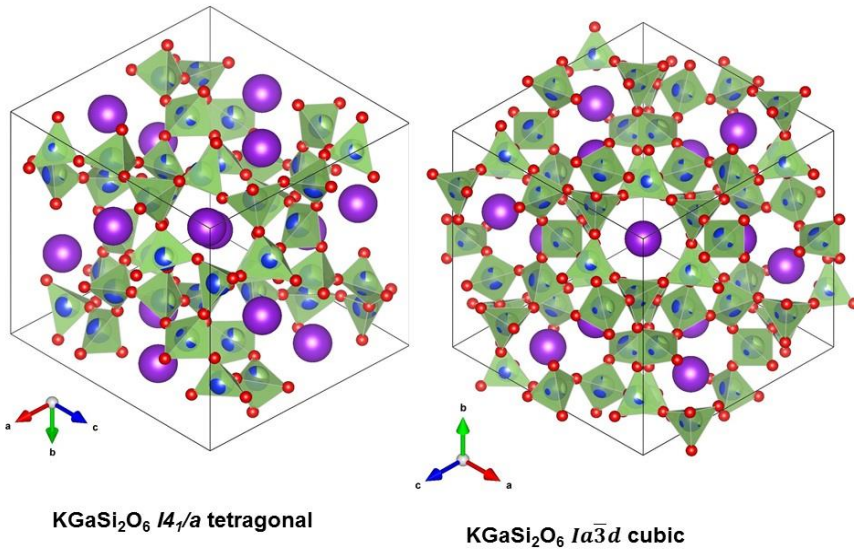


Figure 7. Crystal structure plots for KGaSi₂O₆ *I*4₁/*a* tetragonal and *Ia* $\bar{3}$ *d* cubic phases. Purple spheres represent K⁺ cations, green and blue spheres represent disordered Si⁴⁺/Ga³⁺ cations, red spheres represent O²⁻ anions and green tetrahedra represent (Si,Ga)O₄ units. COLOUR FIGURE.

Palmer et al. [28, 30] calculated the strain associated with displacive phase transitions in the leucite structure by relating the measured *a* and *c* parameters at particular temperatures below the phase transition to those for the cubic polymorphs extrapolated to these lower temperatures (*a*₀ values). They also calculated model mean ‘cubic’ parameters from the tetragonal data at each temperature (i.e., (2*a*+*c*)/3; *a*₀’). They pointed out that for a pure ferroelastic transition *a*₀ and *a*₀’ values should be identical. We have calculated values for *a*₀ in KGaSi₂O₆ leucite as a function of temperature from cubic phase cell edges at 673 to 1073 K; this fit gave the equation *a*₀ (Å) = 0.000338 * temperature (K) + 13.2601 (R² 0.979). In Figure 8a we show the measured unit cell parameters for the KGaSi₂O₆ leucite as a function of temperature; also shown are the extrapolated *a*₀ and calculated *a*₀’ values. It is clear that at low temperatures the *a*₀ points are very close to those for *a*₀’ but through the region of coexistence the two sets of data diverge slightly. We also used the method of Palmer et al. [30] to calculate volumes for a purely ferroelastic transition (*V*_e) where *V*_e = (27*V*₀*a*²*c*)/(2*a* + *c*)³ and *V*₀ is the cubic volume extrapolated to lower temperatures [28, 30]. Figure 8b shows the plot for the volume parameters as a function of temperature; note that measured volumes for coexisting tetragonal and cubic phases at 773 and 873 K are both plotted. The very small displacement of *V*₀ from *V*_e values (0.09%) is consistent with the transition for KGaSi₂O₆ leucite being close to pure ferroelastic with a very small volume-changing strain but it seems that close to the end of the phase transition the volume strains tends to increase. The implication is that the transition is close to being purely ferroelastic but other strains are

evident and we have investigated this further with the more-detailed approach used by Palmer et al. [28, 30] and the later contribution by Carpenter et al. [35].

Palmer et al. [28, 30] defined the spontaneous strains for the tetragonal phases at each temperature below the phase transition in terms of three component strains: the total spontaneous strain, $\epsilon_{\text{total}} = [(c - a_0)/a_0]^2 + 2(a - a_0)/a_0^{1/2}$; the non-symmetry-breaking volume strain, $\epsilon_a = \sqrt{3} [(a_0 - (c + 2a)/3)/a_0]$; and the symmetry-breaking ferroelastic strain $\epsilon_e = \epsilon_{\text{total}} - \epsilon_a$. These equations were superseded by those of Carpenter et al. ([35] who defined a symmetry breaking strain (e_t) as: $e_t = 1/\sqrt{3}(2e_{33} - e_{11} - e_{22})$ (their equation 29); a non-symmetry breaking strain (e_{33}) was defined as: $e_a = e_{11} + e_{22} + e_{33}$ (their equation 30). For a tetragonal/cubic transition: e_{11} and $e_{22} = (a_T - a_0)/a_0$ (cf. equation (55)) and $e_{33} = (c_T - a_0)/a_0$ (cf. equation (57)) where T defines the temperature of cell edge measurements. The Carpenter tetragonal strain [35] therefore is defined as $e_t = (1/\sqrt{3})(2e_{33} - 2e_{11})$ and the measured volume strain (V_s) is given as: $V_s = (V_T - V_T^0)/V_T^0$. Note that all of these strain equations are defined using the same variables (i.e., tetragonal unit cell edges a , c and the a_0 values extrapolated from the cubic polymorph values).

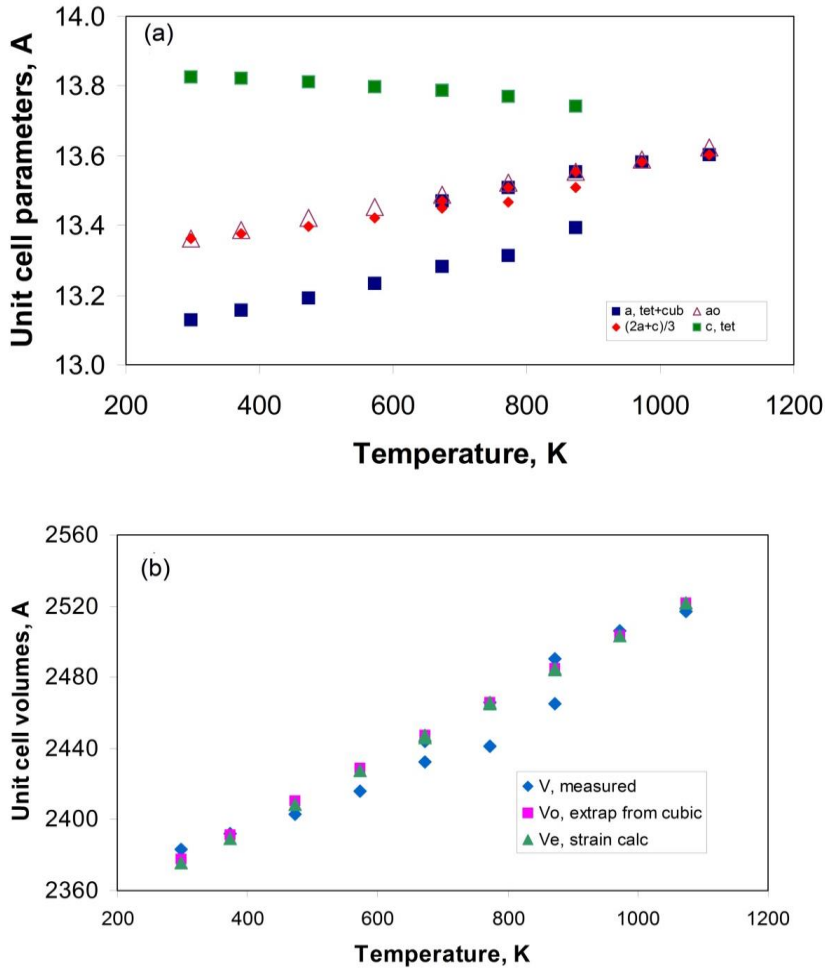


Figure 8. Figure 8a, Dependence of KGeSi₂O₆ measured cell parameters a and c on temperature; also plotted are a_0 parameters calculated by extrapolating the high-temperature cubic polymorph edges to lower temperatures [28, 30, 35] and the model unit cubic cell edges (a_0 , $(2a+c)/3$) [28, 30, 35] calculated assuming a purely ferroelastic phase transition; Figure 8b, dependence of KGeSi₂O₆ measured cell volumes on temperature, also plotted are the measured volumes for cubic phases at high temperature extrapolated to lower temperatures in the tetragonal stability field together with the volumes calculated assuming a purely ferroelastic transition [30]. See text for explanation. COLOUR FIGURE.

The strain parameters calculated using the equations of Carpenter et al. [35] for the tetragonal polymorphs of KGeSi₂O₆ are shown in Figure 9a and b using per mil units; all the cubic polymorphs plot on the zero e_t axis. It is clear that the tetragonal strain vs temperature data at up to 773 K define an excellent linear trend

and even the point at 873 K falls close to this trend ($e_t = -0.0513 \times T + 77.02$). The tetragonal phases defining the top three temperature points all fall within the region of coexistence and the matching cubic phase data points are also shown (Figure 9a) for these temperatures and this serves to show the discontinuity between the tetragonal and cubic structures for KGaSi_2O_6 . The volume strains (V_s) for all the tetragonal phases are uniformly small ranging from 2 % at 298 K to – 10 % at 773 K (Figure 9b). The e_t vs V_s parameters are plotted in Figure 9b and define a good linear trend with only the highest temperature point deviating from that trend (see later discussion). Carpenter et al. [35] show that e_t and V_s calculated for Palmer's data [30] for natural KAlSi_2O_6 demonstrate an excellent linear relationship for that sample. Note that the volume strains for KGaSi_2O_6 leucite are all about 30 times smaller than those for KAlSi_2O_6 leucite consistent with our earlier conclusion that KGaSi_2O_6 leucite is closer to being purely ferroelastic than KAlSi_2O_6 leucite. Figure 9a also shows our calculated data for the symmetry-breaking ferroelastic tetragonal strain using the published unit cell parameters for KAlSi_2O_6 [30], $\text{KFe}^{3+}\text{Si}_2\text{O}_6$ leucite, $\text{RbAlSi}_2\text{O}_6$, $\text{CsAlSi}_2\text{O}_6$ leucites [28] and $\text{Cs}_2\text{Ti}_{0.1}\text{Al}_{0.9}\text{Si}_2\text{O}_{6.05}$ (Xu et al., [52]). The e_t vs temperature data for the $\text{CsAlSi}_2\text{O}_6$ and $\text{RbAlSi}_2\text{O}_6$ analogues all have well-defined flat curves which show clear intersections with the zero-strain axis; these provide well defined transition temperatures to cubic symmetry (T_c). Palmer et al [28] and Xu et al. [52] showed that the squared spontaneous strains versus temperature plots for the $\text{CsAlSi}_2\text{O}_6$ and $\text{RbAlSi}_2\text{O}_6$ analogues plot define good linear trends and concluded that the phase transitions for those samples were close to tricritical. The structural data for the KFeSi_2O_6 and KAlSi_2O_6 leucites differs somewhat from those for the $\text{CsAlSi}_2\text{O}_6$ and $\text{RbAlSi}_2\text{O}_6$ analogues. Thus Palmer et al. [28] have pointed out that the mean cavity cation to oxygen distances against the cube root of volumes (i.e. the mean cell edge for the pseudocubic structure) at different temperatures for $\text{KFe}^{3+}\text{Si}_2\text{O}_6$ and KAlSi_2O_6 leucites show clear **discontinuities** between the trends for the tetragonal and cubic phases while those for the $\text{CsAlSi}_2\text{O}_6$ and $\text{RbAlSi}_2\text{O}_6$ leucites merge. Thus, Figure 9a shows smoothly curved spontaneous strain trends for $\text{KFe}^{3+}\text{Si}_2\text{O}_6$ and KAlSi_2O_6 which at the highest temperatures are very steep but do not intersect the zero axis; this reflects the structural discontinuities between the tetragonal and cubic phases referred to above for these samples [28]. Nevertheless, the extrapolated trends for the $\text{KFe}^{3+}\text{Si}_2\text{O}_6$ and KAlSi_2O_6 leucites have clearly defined T_c intercepts. The data we have plotted here for natural leucite includes both Palmer's powder neutron diffraction data [28] as well as the powder XRD data published and discussed by Palmer et al. [30]. From Figure 9a it is clear that at temperatures up to about ~ 770 K the KGaSi_2O_6 , KAlSi_2O_6 and $\text{KFe}^{3+}\text{Si}_2\text{O}_6$ leucites all fall within the same spontaneous strain 'band' but diverge significantly at higher temperatures. Palmer et al. [30] commented that the squared symmetry-breaking spontaneous ferroelastic strain (ϵ_e) trend versus temperature for natural leucite is very close to linear up to ~ 500°C (~750 K) consistent with a second order Landau free energy expansion ($\beta = 1/2$) (see Palmer et al., Figure 4b, [30]). We have also used Palmer's strain equations to compare the squared epsilon strains data (ϵ_e , ϵ_a , and ϵ_{Tot}) versus temperature for our KGaSi_2O_6 sample to those for Palmer *et al's* XRD data for KAlSi_2O_6 [30, 31] and Palmer *et al's* (1997)

neutron data for KAlSi_2O_6 and $\text{KFe}^{3+}\text{Si}_2\text{O}_6$ [28] and show the results in (Figure 10 a,b,c). The lower $(\epsilon_{\text{total}})^2$ values for KGaSi_2O_6 suggest that it is less distorted than KAlSi_2O_6 and $\text{KFe}^{3+}\text{Si}_2\text{O}_6$ leucites; note also the very low volume strains for KGaSi_2O_6 (Figure 10c). Although the trends for KAlSi_2O_6 are slightly different for the neutron and XRD data sets (mainly resulting from the different extrapolation fits from the cubic cell parameters) the squared non-ferroelastic volume strain ϵ_a and squared total strains ϵ_{Tot} versus temperature trends are more curved (downwards) for all three $\text{KY}^{3+}\text{Si}_2\text{O}_6$ ($Y = \text{Al}, \text{Fe}, \text{Ga}$), than for the squared ferroelastic strains ϵ_e , which for all samples are almost linear up to 750-800 K. Thus on that basis all three species have features consistent with a second order transition yet Palmer *et al* [28] concluded that the transition for $\text{KFe}^{3+}\text{Si}_2\text{O}_6$ leucite is first order and it is clear that the region of coexistence and a volume discontinuity found for KGaSi_2O_6 leucite are also indicative of first order behaviour. We will return to this in the final section (see section 3.1.4).

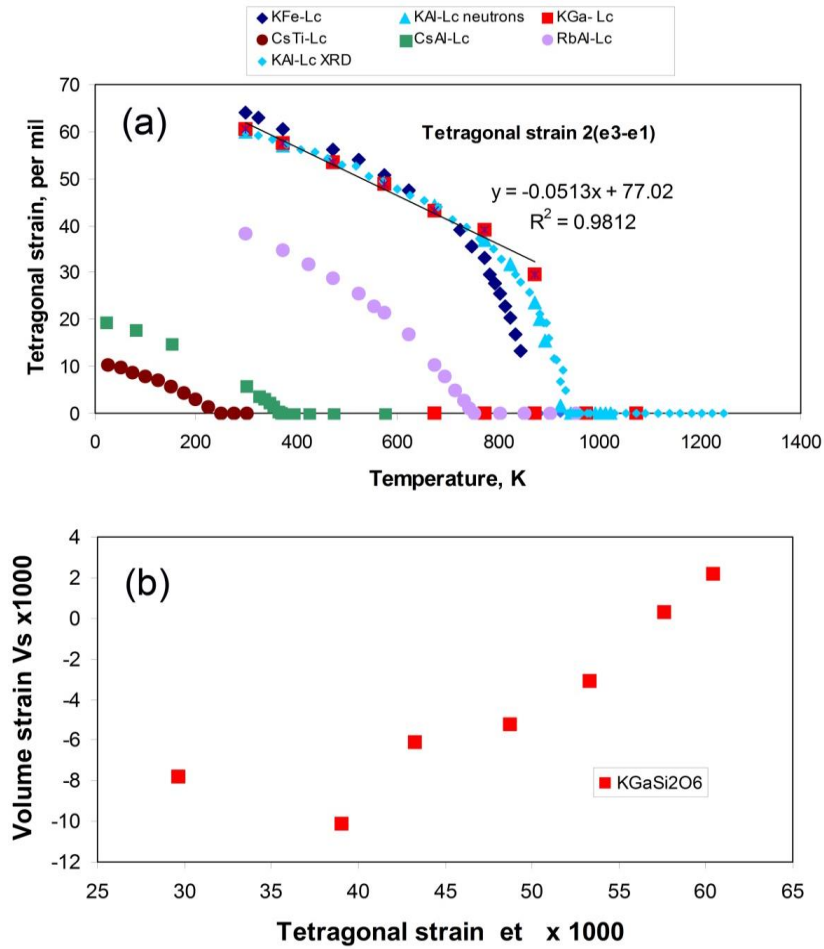


Figure 9. Figure 9a, Calculated tetragonal strain parameters (e_i) [35] as a function of temperature for KGaSi_2O_6 (this work) and for: KAlSi_2O_6 [28, 30, 31], $\text{RbAlSi}_2\text{O}_6$ [28], $\text{CsAlSi}_2\text{O}_6$ [28], $\text{KFe}^{3+}\text{Si}_2\text{O}_6$ [28] and $\text{CsAlTi}_2\text{O}_6$ [52]. The linear dependence on temperature is shown for the tetragonal KAlSi_2O_6 polymorphs. Figure 9b, Calculated volume strain (V_s) versus ferroelastic tetragonal strain [35] for KGaSi_2O_6 . COLOUR FIGURE.

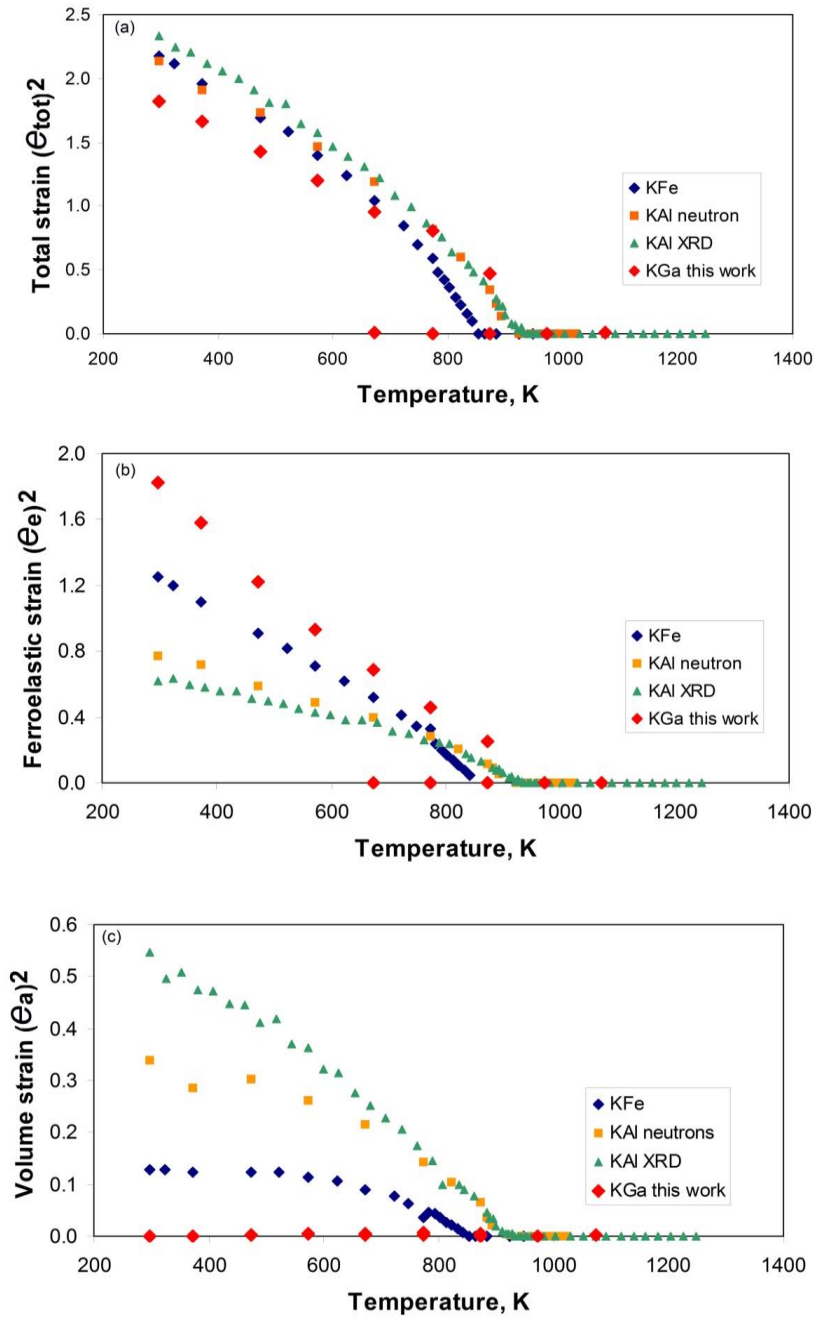


Figure 10. Dependence of the strains (squared) defined by Palmer et al. [28, 30] on temperature for KGaSi₂O₆ (this work), KAlSi₂O₆ [28, 30, 31], and KFe³⁺Si₂O₆ [28]. Figure 10a, total strain $\epsilon_{\text{total}}^2$ vs T ,

Figure 10b ferroelastic strain ϵ_e^2 vs T , Figure 10c volume strain ϵ_a^2 vs T , note the very small volume strain for KGaSi_2O_6 . See text for explanation. COLOUR FIGURE.

3.1.2. Characteristics of the phase transitions in *K-leucites*.

High temperature X-ray single crystal and powder diffraction [24,25,27,30,53] and powder neutron diffraction [28] studies on leucite KAlSi_2O_6 all show a continuous and reversible $I4_1/a$ to $Ia\bar{3}d$ displacive phase transition during heating at very similar temperatures of $\sim 930\text{K}$, but **no two-phase** region was reported for this transition for any of these natural, stoichiometric K-leucite samples. Due to the continuous transition from tetragonal to cubic symmetry for the natural leucites it is clear that there can be no volume discontinuity ($\Delta V = 0$) at the transition. However, Henderson and Taylor [48] pointed out that some synthetic and natural silica-rich K-leucites showed regions of coexistence of tetragonal and cubic phases over a range of temperature together with positive ΔV values ($V_{\text{cubic}} > V_{\text{tetrag}}$) through the transition similar to those we have now found for synthetic KGaSi_2O_6 . Redfern and Henderson [37] studied the ferroelastic phase transition for $\text{K}_2\text{MgSi}_5\text{O}_{12}$ $P2_1/c$ leucite and showed a similar behaviour in that monoclinic and *Pbca* orthorhombic phases coexisted over a temperature range of at least 30K for the reversible first-order ($\Delta V +1.6\%$) transition to *Pbca*. We will explore the implications of such differences to the mechanism of the crystallographic phase transition occurring in $I4_1/a$ leucite varieties in the final section of this paper.

3.2 Does leucite display an athermal, martensitic-type phase transition?

3.2.1. Phase transformations in framework silicate and analogous compounds.

Over several decades one of us (CMBH) studied the thermal expansion and displacive phase transitions shown by natural and synthetic analogues having ‘stuffed’ silicate frameworks belonging to the leucite/pollucite, nepheline/kalsilite, sodalite, and feldspar mineral groups (see Supplementary Information file). Of particular relevance here is the paper on the system $\text{SrAl}_2\text{O}_4 - \text{BaAl}_2\text{O}_4$ (Henderson and Taylor, 1982) [48] which dealt with the displacive phase transition (monoclinic to hexagonal) shown by monoclinic solid solutions in this system which have crystal structures very similar to the nepheline-kalsilite mineral group $[(\text{Na},\text{K})\text{AlSiO}_4]$. At room temperature, samples in the series $(\text{Sr}_{1-x}\text{Ba}_x)\text{Al}_2\text{O}_4$ with x in the range 0 to 0.31 are monoclinic, those with x varying 0.31 to 0.43 consist of mixtures of monoclinic and hexagonal phases, while those with $x > 0.43$ are all hexagonal. During heating, monoclinic Sr-rich solid solutions begin to transform to the hexagonal polymorph but this ‘smeared’ transition takes place over a range of temperature within which both ‘low’- and ‘high’ forms coexist; for SrAl_2O_4 the transformation has a negative volume change of -0.26% . On cooling, the reverse transition takes place with a marked hysteresis. Henderson and Taylor [48] called the two-phase mixtures the ‘region of coexistence’; this region was mapped out on a temperature – composition diagram and shows that the thermal width is smallest for the Sr end member (938 to 978K) and wider for more-Ba rich compositions (e.g., for $\text{Sr}_{0.7}\text{Ba}_{0.3}\text{Al}_2\text{O}_4$ it is 443K to

678K). Henderson and Taylor (1982) [48] compared this type of behaviour to those described for the tetragonal – cubic thermal transition displayed for cristobalite (SiO₂) (Leadbetter and Wright, 1976; ΔV 4%) [54] and to the diffusionless monoclinic-hexagonal phase transformation exhibited by ZrO₂ (Wolten, 1963; ΔV 3-5%) [55]. Thus, they concluded that the phase transformation for the Sr-Ba aluminates is first-order, displacive, athermal, both phases have the same chemical composition, mediated by strain, and with features suggestive of a martensite-like mechanism. In the final section of their paper on the Sr-Ba aluminate system Henderson and Taylor [48] discussed the implications of these results to sodic nephelines and potassic leucites and reported preliminary data for silica-rich leucites (cf. Henderson, 1981) [56]. The latter samples showed tetragonal to cubic transitions involving two-phase regions similar to those reported here for Sr-Ba aluminates and to those for KGaSi₂O₆ described in the present paper and in the final section we will assess likely mechanisms for K-rich leucites having variable composition silicate frameworks.

3.1.2. *Smearred tetragonal – cubic transformations in K- leucites.*

The data for the different samples are summarized in Table 4. Note that the silica-rich leucites are reported as having orthoclase (K-feldspar) in solid solution. The feldspar end member formula, KAlSi₃O₈, recalculated on a leucite cell basis would be K_{0.75}□_{0.25}Al_{0.75}Si_{2.25}O₆, where □ refers to vacancies in the cavity cation site (Henderson et al., [18]). The synthetic samples are prepared from either ground glass or powdered gel starting materials (Hamilton and Henderson, 1965) [57]. Natural leucite 28054 (Taylor and Henderson, 1968) [25] is essentially stoichiometric KAlSi₂O₆ with small amounts of Na replacing K and Fe³⁺ replacing Al. Natural leucite A.1776 (Carmichael, 1967; Lange et al., 1986) [58, 29] is very unusual in having comparatively high silica contents [reported as the Or feldspar molecule] and Fe³⁺ replacing Al. Synthetic samples KGa-Lc, KLc1 and HL.26 were all prepared from stoichiometric starting compositions [K(Al or Ga)Si₂O₆] in air at the temperatures and times shown in Table 4. Synthetic samples L.60 and L.110 have different amounts of K-feldspar in solid solution and both were prepared hydrothermally at the pressures, temperatures and times shown (see also MacKenzie et al., [59]). Samples of framework silicates synthesized in air (dry) tend to be less well crystalline (more disordered) than hydrothermally synthesized phases. Natural leucites usually provide well crystalline samples. The X-ray diffraction peak widths at half maximum height (FWHM, Table 4) refer to peaks over the range 20 to 30° 2θ (CuK_α) and show that KLc1 (data from Taylor and Henderson, [25]) is the least well crystalline sample with HL.26 (KLc2, Henderson et al., [18]) being slightly more ordered. KGaLc1 (this paper), the two hydrothermally synthesized samples (L.60, L.110) and natural leucite A.1776 are all much better crystalline and the best sample is the natural leucite 28054 with good sharp peaks. Clearly the samples with broader peaks show much more pronounced overlapping of peaks ((400)_t, (004)_t, and (400)_c; subscripts t and c refer to peaks for the tetragonal and cubic phases, respectively) in any region of coexistence.

Note that the first appearance of the cubic phase is clear with good separation between the peaks for the two phases (Figure 1). Volumes are reported for the coexisting phases at 873 K (Table 4) and show a positive ΔV of 1.0 % on heating; no data were obtained for cooling experiments.

Inspection of the original XRD charts for natural leucite 28054 shows no sign of the appearance of a $(400)_c$ peak before the $(400)_t$ and $(004)_t$ begin to overlap. A simple transition of 993 K on heating and 983 K on cooling can be identified; these values are slightly higher than the temperatures adopted by Taylor and Henderson [25] and the transition is continuous with no region of coexistence. A similar situation is clear for the well crystalline, hydrothermal L.60 despite it being slightly silica rich (Or_4) and the same transformation temperatures were assigned for this sample for both heating and cooling cycles (Table 4). It seems that for these two samples the evidence suggests that the phase transition is continuous, displacive and 2nd order with no ΔV as reported for natural K-leucite (see earlier). However, despite the much broader peaks for end-member synthetic KLC1, a small peak for a cubic phase appeared at about 650 K and this shows an increase in intensity before the $(400)_t$ and $(004)_t$ peaks overlap with it. The completion of the transformation is assigned to the temperature (890 K) when the final $(400)_c$ peak had its maximum intensity, the most symmetrical peak shape and with the smallest FWHM. Tentative unit cell volumes for the coexisting phases at 790 K are given in Table 4 with a ΔV of ~0.6%. Sample HL.26 has the same nominal composition as KLC.1 and is better crystallized so that the region of coexistence observed is much better defined from 810 to 920 K on heating and from 980 to 720 K on cooling with a clear hysteresis of 60 K. Volumes for the coexisting tetragonal and cubic phases at 870 K and a ΔV of 0.5% are reasonably well defined. Synthetic, hydrothermal, silica-rich K-leucite (Or_{30}) and natural leucite A.1776 (Or_{12}) show similar regions of coexistence, similar degrees of hysteresis, and similar ΔV values of 1.0% (measured at 800 K) and 0.8% (at 735 K), respectively (Table 4). For these four samples and for the $KGaSi_2O_6$ sample it seems that the tetragonal to cubic transformation has a different mechanism to those given above for natural K-leucite.

3.1.3. Characteristics of diffusionless ferroelastic phase transitions.

In this section we will summarise the most significant characteristics for diffusionless phase transitions ((e.g., Fultz, [60]) based on published work on tetragonal/cubic SiO_2 -cristobalite, monoclinic/tetragonal zirconia, and tetragonal/cubic $BaTiO_3$, in an attempt to pin down the micro- and macro-structural factors influencing the nature of the unquenchable tetragonal-cubic transition in K-leucites. The characteristics for the phase transitions for these three materials are summarised in the Supplementary Information file (section S.4) with only the key findings summarised here.

It is clear that the phase transitions for cristobalite, zirconia, and $BaTiO_3$ all show very similar properties. Thus, all those diffusionless transitions are ferroelastic, fully reversible, show hysteresis, occur very fast, commonly show ranges of temperature with both phases coexisting, and significant shape differences between unit cells for the low- and high-temperature polymorphs; in addition, the cristobalite and zirconia

transitions are associated with substantial ΔV 's. All three ferroelastic systems show the formation of transformational multiple twins on cooling from the high-T (untwinned) polymorphs driven by the symmetry breaking changes and the strain associated with the phase transition. The properties of the phase transitions in both ZrO_2 and BaTiO_3 can be explained by similar short and medium range order mechanisms. However, the situation for the natural sample of cristobalite is complicated by the possibility of some Al replacing Si in the framework and Na entering interframework cavities in variable amounts to produce stuffed-cristobalite analogues rather than the SiO_2 end-member [61]. However, we prefer to assume that the α - β transition in pure cristobalite is also mediated by strains associated with the coexistence of the two phases together with a significant ΔV ($\sim 4\%$) suggesting that it too shows martensitic characteristics.

Based on the characteristics of the phase transition observed for ZrO_2 and BaTiO_3 it is clear that the effective size of the diffracting crystallites will influence the temperature of a martensitic-type phase transition, and the wider the range of crystallite sizes in a powder, the wider would be the temperature range of the region of coexistence (see Supplementary File, Table S.1). In addition, the greater the unit-cell shape difference between the coexisting polymorphs and the larger the ΔV of the transformation, the greater the importance of any strain energy within the powder particles as was pointed out many years ago (e.g., Wolten [55]). Indeed, the smaller the nanoparticle the larger the role played by its greater surface strain energy would be. The length scale and complexity of the ubiquitous transformation twin domains in the lower temperature polymorph might also play an important role by affecting the progression of the athermal transition mechanism which controls the gradual release of the strain within the particles as the temperature increases.

3.1.4. Mechanism of the tetragonal to cubic phase transition in *K-leucites*

The implications of the detailed research on ZrO_2 and BaTiO_3 phase transition covered in the Supplementary Information section to the leucite phase transition are clear. Table 4 shows for end-member KLC100 samples, that the less well crystallized sample (KLC1) has a much wider two-phase region than the better crystalline sample (HL.26), i.e. ~ 240 and 110 K, respectively. However, the better crystalline synthetic (L.110) and natural (A.1776) also have wide two-phase regions (120 and ~ 150 K, respectively) and the width for the well crystalline KGaSi_2O_6 sample is even larger at ~ 225 K. It seems to be more likely that the differences could reflect differences in the ranges of the effective crystallite sizes, the bigger the range the wider the two-phase region, and the smaller the sizes, the lower the temperature at which the tetragonal to cubic transition would begin. Note also that, in contrast to the stoichiometric leucites the silica-rich KAl-leucites and the KGaSi_2O_6 leucite have large ΔV values (up to 1%) and the significant shape differences for the coexisting tetragonal and cubic phases (e.g. c/a 1.04 vs 1.0 for KGaSi_2O_6 , Table 1) would be expected to be more affected by strain properties of the component powder grains.

Using the new diffraction data for KGaSi_2O_6 we have assessed how the effective crystallite grain size (i.e., the coherently diffracting domain size) might influence the characteristics of the tetragonal cubic phase transition in leucites. The Scherrer [62, 63] equation was used to estimate this size parameter from the measured peak widths for the (004) and (400) peaks in KGaSi_2O_6 and the results are given in Table 4; the average for the two peaks is ~ 90 nm, which can be compared with a powder particle size varying from ~ 20 μm , down to at least 200 nm.

For comparison with this new sample we have looked again at the powder samples used to characterise the phase transition for natural leucite (28054, Taylor and Henderson [25]) and a synthetic leucite (HL26, Henderson [54]). Natural leucite 28054 mainly occurs as 0.5 to 1 cm phenocrysts in a nosean leucitophyre from Rieden, Germany, and the crushed powder used for the XRD work is made up of angular clear fragments, birefringent but generally untwinned grains (10-20 μm) together with smaller particles some of which are twinned. The former grains are likely to be from within wide twin lamellae in the host phenocryst. Sample HL.26 is similar to the KGaSi_2O_6 leucite sample. Lamproites from the Leucite Hills, Wyoming, A.1776 (Carmichael, 1967; LH.14) and A.128 (LH.7) [58] do not contain leucite as phenocrysts and it typically occurs in the quenched groundmass as grains ranging 5 to 60 μm which are described as being untwinned and completely isotropic [58, 64]; Carmichael [58] originally assumed that these were cubic which had been quenched from above the leucite phase transition. Note that heating XRD experiments on the Leucite Hills samples were carried out on crushed bulk rock samples and showed that the leucites were indeed tetragonal at low temperatures.

Samples of the original powder samples of K-leucites 28054 and HL.26 have also been used to obtain crystallite sizes from the FWHM values for (004) and (400) peaks (Table 4); average crystallite sizes of 345 and 200 nm, respectively, were obtained. The FWHM values measured for 28054 and HL.26 peaks using the PANalytical X-Pert Pro MPD at Sheffield Hallam University are almost identical to those estimated from the Philips PW1050 original X-ray powder diffraction charts [54] for the same samples (Table 4). The newly determined FWHM vs crystallite size values for 28054 and HL.26 were then used to estimate crystallite sizes for the other leucite samples given in Table 4. Thus for KLC1, L.60, L.110, and Leucite Hills sample A.1776, this calibration gives average crystallite sizes of 136, 210, 200, and 200 nm, respectively. We expect errors for these 'average' values might be $\sim 50\%$ and it seems likely that these data represent the averages of wide crystallite size ranges for each sample. Note that samples HL.26, L.110, and A.1776 all have similar crystallite size values (200-210 nm) and all show similar temperature ranges over which the tetragonal/cubic phase transition occurs (110 to 150 K). In comparison, sample KLC1 shows a wider temperature range for the transition (240 K) which is matched by its smaller average crystallite size (136 nm). We conclude that all these samples have wide ranges of crystallite sizes with sample KLC1 having a larger population of the smallest sizes of crystallites which, in turn, is responsible for the phase transition being initiated at a lower temperature.

Of course, each powder particle in a sample could consist of intimate intergrowths of microstructural domains (e.g., Frey et al. [65]); thus, individual grains in the powder samples of our synthetic leucites and fine-grained natural Leucite Hills sample could host domains of different sizes with different degrees of crystallinity and with different degrees of strain.

In addition, the length scale and texture of the twin domains could play a part in the progression of the athermal transition in leucites. As mentioned in the introduction it is well known that leucite shows a well-developed ‘memory’ regarding the twin distribution and nature during thermal cycling through the transition. This implies some structural control of the siting of twin boundaries even though the silicate framework is coherent across the twin boundaries. Although the width of twin lamellae is frequently around 100 to 300 nm for pseudo-merohedral and merohedral twins in natural leucite, finer grained tweed/cross-hatched twins are also known. In addition TEM studies of intersecting twin lamellae show highly strained features together with structural discontinuities and defect-rich regions (Palmer and Salje [35]; Heaney and Veblen [32]) which could be considered as reducing the effective sizes of the crystallites that scatter X-rays. Indeed Salje [66, 67] has pointed out that domain boundaries, including twin walls and other interfaces, can modify the macroscopic properties of materials which could be exploited for engineering purposes. Such features might modify the way a transition wave could sweep through a composite or twinned grain during a ferroelastic strain-related transformation. However, one of the natural leucite samples studied by Palmer and Salje [35] is the leucite from Rieden, Germany (Harker Collection number L28054) which is the same sample that Taylor and Henderson [25] used; this sample shows continuous evolution without any region of coexistence. It seems that microstructures associated with the characteristic twinning in leucite are not the principal control of the martensite-like properties.

At 298 K the a and c cell edges for KGaSi_2O_6 are both slightly larger than for those for KAlSi_2O_6 [25, 28] but slightly smaller for $\text{KFe}^{3+}\text{Si}_2\text{O}_6$ [28] consistent with the increasing ionic radii for 4-coordinated Al, Ga and Fe^{3+} [47]. However, all three K-leucites have similar c/a ratios (KAlSi_2O_6 1.054, KGaSi_2O_6 1.053, $\text{KFe}^{3+}\text{Si}_2\text{O}_6$ 1.056). The KAlSi_2O_6 , $\text{KFe}^{3+}\text{Si}_2\text{O}_6$ and KGaSi_2O_6 leucites all show similar behaviour in the initial stages of thermal expansion from room temperature up to 750 K and this is reflected in the calculated strain parameters showing a close to linear dependence over this temperature range. These different leucites all show similar rates of change of the tetragonal c/a ratios from 298 to 750 K (KAlSi_2O_6 1.054 to 1.038; $\text{KFe}^{3+}\text{Si}_2\text{O}_6$ 1.056 to 1.031; KGaSi_2O_6 1.053 to 1.036); the mean relative change over 450 K is 2.0(3) %. From 670 K to the different T_c s the c/a changes are 3.1, 2.9, and 3.4 %, respectively; the average is 3.0(3) % occurring over a mean temperature difference of 150 K. Thus, the rate of change of c/a with increasing temperature during the main structural transition is about 5 times more rapid than for the initial thermal expansion stage which has been correlated with a 2nd order mechanism [28]. However, Palmer et al. [28] suggested that the discontinuities between the tetragonal and cubic phase of KAlSi_2O_6 and $\text{KFe}^{3+}\text{Si}_2\text{O}_6$ leucites close to T_c could indicate either first-order transition characteristics or an additional mechanism near the T_c ; for KAlSi_2O_6 they correlated the latter with the prominent ferroelastic shear distortion associated

with an $Ia\bar{3}d$ to $I4_1/acd$ stage for the transition but overall the transition was considered to be continuous and 2nd order for the naturally occurring mineral. For KGaSi_2O_6 we have concluded that the tetragonal to cubic structural change occurs via a first order martensitic-type transition. It seems that the types of distortion and strains within the different natural and synthetic leucites have a similar nature although different samples overcome the effects of the strains by different mechanisms. Natural leucite is able to undergo a continuous 2nd order transition via the formation of the intermediate $I4_1/acd$ phase; this transition has been shown to occur in many examples of natural phenocrystic leucite and might be expected to be the ‘normal’ mechanism. However, we suggest that the synthetic KGaSi_2O_6 and silica-rich KAl-leucites and the natural silica-rich Leucite Hills groundmass leucites at temperature close to the phase transition are able to reduce the internal strain within the tetragonal phase more easily by nucleating the cubic polymorph and then, as the temperature continues to change, the athermal nature of the transition allows the proportion of the high-temperature cubic phases to increase to completion without formation of an intermediate phase. The result is that the tetragonal phase is generally less strained throughout the temperature range with a distinct ΔV and other first order transition characteristics related to micro- and nano-structural features. Such features would be influenced by the presence of small grains having high surface energies and/or larger grains with complex domain structures and defect rich sub-grain boundaries.

4. Conclusions

At room temperature the leucite analogue KGaSi_2O_6 has the tetragonal $I4_1/a$ structure which is the same structure as that of natural leucite KAlSi_2O_6 [1, 28] and synthetic $\text{KFe}^{3+}\text{Si}_2\text{O}_6$ [28]. At 298 K the a and c cell edges for KGaSi_2O_6 are both slightly larger than those for KAlSi_2O_6 [25, 28] but slightly smaller than those for $\text{KFe}^{3+}\text{Si}_2\text{O}_6$ [28] consistent with the increasing ionic radii for 4-coordinated Al, Ga and Fe^{3+} . However, all three K-leucites have similar c/a ratios (KAlSi_2O_6 1.054, KGaSi_2O_6 1.053, $\text{KFe}^{3+}\text{Si}_2\text{O}_6$ 1.056).

At elevated temperatures the KGaSi_2O_6 unit cell expands and the c/a decreases until at 673 K a second leucite phase appears alongside the tetragonal polymorph; the new leucite phase has the cubic $Ia\bar{3}d$ structure [2] and the proportion of this phase increases with increasing temperature until at 973 K the tetragonal phase is no longer detectable. Differential Thermal Analysis (DTA) on KGaSi_2O_6 shows a change in the DTA curve in the approximate temperature region 600-900 K, this is close to the two-phase region observed by XRD. The temperature range over which two leucite phases coexist is denoted the ‘region of coexistence’; the cubic phase has a larger cell volume than the coexisting tetragonal phase with a ΔV of ~0.8-1.0%. The proportion of the two phases changes **instantaneously** with changing temperature and at a fixed intermediate temperature the phase proportion is fixed pointing to an athermal, isochemical mechanism [56]. Some synthetic stoichiometric KAlSi_2O_6 leucites, non-stoichiometric synthetic silica-rich leucite, and natural silica-rich leucites from Leucite Hills lamproites [58] show similar tetragonal to cubic phase transitions smeared out over a range of temperature and all show positive ΔV s similar to that for KGaSi_2O_6 . Such features are characteristic of 1st order, diffusionless, athermal, reversible, strain-mediated, martensitic

phase transitions. The temperature dependence of ferroelastic strains associated with the leucite phase transition for KGaSi_2O_6 are calculated and show that the symmetry-breaking tetragonal strains [35] are similar at low temperatures for all three KAlSi_2O_6 , KGaSi_2O_6 and $\text{KFe}^{3+}\text{Si}_2\text{O}_6$ leucites but the non-symmetry-breaking volume strain for KGaSi_2O_6 leucite is much smaller than those for the KAlSi_2O_6 and $\text{KFe}^{3+}\text{Si}_2\text{O}_6$ samples consistent with the tetragonal to cubic transition for KGaSi_2O_6 being close to being purely ferroelastic in character. The smeared-out phase transition reported for KGaSi_2O_6 leucite, synthetic silica-rich leucite, and natural silica-rich groundmass leucites from Leucite Hills lavas is believed to be related to the presence of a range of sizes of the X-ray diffracting crystallites in sub-grain-powder samples. One controlling factor could be due to surface energy properties of a population of nano-particles in the sample stabilising the higher symmetry structures to abnormally low temperatures as has been shown for ZrO_2 and BaTiO_3 (see attached Supplementary File).

CRedit author statement

Conceptualisation. Anthony Bell and Michael Henderson.

Sample preparation. Data collection and analysis. Original Draft of paper. Anthony Bell

Revised Draft of paper and literature review Michael Henderson.

Acknowledgements. In particular we thank Dr. Kevin Knight for his advice on dealing with strain parameters, for providing general crystallographic expertise, and for his patient assessment of early and later version of this paper. We also wish to thank colleagues from Sheffield Hallam University for their assistance, Paul Allender for Scanning Electron Microscopy work and Dr. Francis Clegg for Differential Thermal Analysis work. Two anonymous referees provided constructive comments which we have incorporated in this revised paper.

This research did not receive any specific grant from funding agencies in the public, commercial, or not-for-profit sectors.

Declarations of interest: none

References.

- [1] F. Mazzi, E. Galli, G. Gottardi, The crystal structure of tetragonal leucite, *Amer. Mineral.* 61 (1976) 108-115.
- [2] R.M. Beger, The crystal structure and chemical composition of pollucite, *Zeits. Krist.* 129 (1969) 280-302. <https://doi.org/10.1524/zkn.1969.129.16.280>
- [3] I. Yanase, H. Kobayashi, Y. Shibasaki, T. Mitamura, Tetragonal-to-cubic structural phase transition in pollucite by low-temperature X-ray powder diffraction. *J. Amer. Ceram. Soc.* 80 (1997) 2693-2695. <https://doi.org/10.1111/j.11512916.1997.tb03175.x>
- [4] K. Yanagisawa, M. Nishioka, N. Yamasaki, Immobilization of cesium into pollucite structure by hydrothermal hot-pressing. *J. Nuclear Sci. Tech.* 24:1 (1987) 51-60. <https://doi.org/10.1080/18811248.1987.9735774>
- [5] H. Mimura, M. Shibata, K. Akiba, Surface alteration of pollucite under hydrothermal conditions, *J. Nuclear Sci. Tech.* 27:9 (1990) 835-843. <https://doi.org/10.1080/18811248.1990.9731261>
- [6] E.J. Lima, L.A. Ibarra, M.A. Vera, V.H. Lara, P. Bosch, S. Bulbulian, Cesium leaching in CsA and CsX zeolites, *J. Phys. Chem.* 108 32 (2004) 12103-12110. <https://doi.org/10.1021/jp048683i>
- [7] G.D. Gatta, R. Rinaldi, G.J. McIntyre, G. Nenert, F. Bellatreccia, A. Guastoni, G. Della Ventura, On the crystal structure and crystal chemistry of pollucite, $(\text{Cs,Na})_{16}\text{Al}_{16}\text{Si}_{32}\text{O}_{96}\cdot\text{H}_2\text{O}$, *Amer. Mineral.* 94 (2009) 1560-1568. <https://doi.org/10.2138/am.2009.3237>
- [8] C. Sanchez-Valle, C-H. Chio, G.D. Gatta, Single-crystal elastic properties of $(\text{Cs,Na})\text{AlSi}_2\text{O}_6\cdot\text{H}_2\text{O}$ pollucite: A zeolite with potential use for long-term storage of Cs radioisotopes. *J. Appl. Phys.* 108 (2010) 093509. <https://doi.org/10.1063/1.3504613>
- [9] L.M. Torres-Martinez, J.A. Gard, A.R. West, Synthesis and structure of a new family of phases $\text{A}_2\text{MGe}_5\text{O}_{12}$: A = Rb, Cs; M = Be, Mg, Co, Zn. *J. Solid State Chem.* 53 (1984) 354-359. [https://doi.org/10.1016/0022-4596\(84\)90112-9](https://doi.org/10.1016/0022-4596(84)90112-9)
- [10] L.M. Torres-Martinez, J.A. Gard, R.A. Howie, A.R. West, Synthesis of $\text{Cs}_2\text{BeSi}_5\text{O}_{12}$ with a pollucite structure. *J. Solid State Chem.* 51 (1984) 100-103. [https://doi.org/10.1016/0022-4596\(84\)90320-7](https://doi.org/10.1016/0022-4596(84)90320-7)
- [11] L.M. Torres-Martinez, A.R. West, New family of silicate phases with the pollucite structure. *Zeits. Krist.* 175 (1986) 1-7. <https://doi.org/10.1524/zkri.1986.175.1-2.1>
- [12] L.M. Torres-Martinez, A.R. West, Pollucite- and leucite-related phases: $\text{A}_2\text{BX}_5\text{O}_{12}$ and ACX_2O_6 (A = K, Rb, Cs; B = Be, Mg, Fe, Co, Ni, Zn, Cd; C = B, Al, Ga, Fe, Cr; X = Si, Ge), *Zeits. Anorg. Allg. Chem.* 573 (1989) 223-230. <https://doi.org/10.1002/zaac.19895730123>
- [13] A.M.T. Bell, C.M.B. Henderson, Rietveld refinement of dry-synthesized $\text{Rb}_2\text{ZnSi}_5\text{O}_{12}$ leucite by synchrotron X-ray powder diffraction, *Acta Cryst.* C50 (1994a) 984-986. <https://doi.org/10.1107/S0108270194002039>

- [14] A.M.T. Bell, S.A.T. Redfern, C.M.B. Henderson, S.C. Kohn, Structures of synthetic $K_2MgSi_5O_{12}$ leucites by integrated X-ray powder diffraction, electron diffraction and ^{29}Si MAS NMR methods. *Acta Cryst. B50* (1994) 31-41. <https://doi.org/10.1107/SO108768193008754>
- [15] A.M.T. Bell, K.S. Knight, C.M.B. Henderson, A.N. Fitch, Revision of the structure of $Cs_2CuSi_5O_{12}$ leucite as orthorhombic *Pbca*. *Acta Cryst. B66* (2010) 51-59.
- [16] A.M.T. Bell, C.M.B. Henderson, Rietveld refinement of the structures of dry-synthesized $MFe^{3+}Si_2O_6$ leucites ($M = K, Rb, Cs$) by synchrotron X-ray powder diffraction. *Acta Cryst. C50* (1994b) 1531-1536. <https://doi.org/10.1107/SO108270194004014>
- [17] A. Martucci, P. Pecorari, G. Cruciani, Dehydration process and transient channel deformations of slightly hydrated boron leucite: An “*in situ*” time-resolved synchrotron powder diffraction study, *Microporous Mesoporous Materials* 142 (2011) 570-576.
- [18] C.M.B. Henderson, A.M.T. Bell, K.S. Knight, Variable stoichiometry in tectosilicates having the leucite/pollucite-type structure with particular emphasis on modelling the interframework cavity cation environment. *J. Solid State Chem.*, 251, (2017) 90-104. [10.1016/j.jssc.2017.04.013](https://doi.org/10.1016/j.jssc.2017.04.013)
- [19] A.M.T. Bell, C.M.B. Henderson, Crystal structures of $K_2[XSi_5O_{12}]$ ($X = Fe^{2+}, Co, Zn$) and $K_2[XSi_5O_{12}]$ ($X = Mn$) leucites; comparison of monoclinic $P2_1/c$ and $Ia\bar{3}d$ polymorph structures and inverse relationship between tetrahedral cation (T = Si and X) – O bond distances and intertetrahedral T – O – T angles. *Acta Cryst. B74* (2018) 274-286. <https://doi.org/10.1107/S2052520618004092>
- [20] A.M.T. Bell, S.A.T. Redfern, C.M.B. Henderson, S.C. Kohn, Structural relations and tetrahedral ordering pattern of synthetic orthorhombic $Cs_2CdSi_5O_{12}$ leucite: a combined synchrotron X-ray powder diffraction and multinuclear MAS NMR study, *Acta Cryst. B50* (1994). 560-566. <https://doi.org/10.1107/SO108768194003393>
- [21] A.M.T. Bell, C.M.B. Henderson, Rietveld refinement of the orthorhombic *Pbca* structures of $Rb_2CdSi_5O_{12}$, $Cs_2MnSi_5O_{12}$, $Cs_2CoSi_5O_{12}$ and $Cs_2NiSi_5O_{12}$ leucites by synchrotron X-ray powder diffraction, *Acta Cryst. C52* (1996). 2132-2139. <https://doi.org/10.1107/SO108270196003162>
- [22] A.M.T. Bell, C.M.B. Henderson, Crystal structures and cation ordering in $Cs_2MgSi_5O_{12}$, $Rb_2MgSi_5O_{12}$ and $Cs_2ZnSi_5O_{12}$ leucites. *Acta Cryst. B65* (2009). 435-444. <https://doi.org/10.1107/SO108768109024860>
- [23] A.M.T. Bell, Henderson, C.M.B., Rietveld refinement of the crystal structures of $Rb_2XSi_5O_{12}$ ($X = Ni, Mn$), *Acta Cryst. E72* (2016) 249-252. <https://doi.org/10.1107/S2056989016001390>
- [24] D.R. Peacor, A high temperature single crystal diffractometer study of leucite, $(K,Na)AlSi_2O_6$. *Zeits. Krist.* 127 (1968) 213-224. <https://doi.org/10.1524/zkri.1968.127.1-4.213>
- [25] D. Taylor, C.M.B. Henderson, The thermal expansion of the leucite group of minerals. *Amer. Mineral.* 53 (1968) 1476-1489.
- [26] M.T. Dove, T. Cool, D.C. Palmer, A. Putnis, E.K.H. Salje, On the role of Al-Si ordering in the cubic-tetragonal phase transition of leucite, *Amer. Mineral.* 78 (1993) 486-492.

- [27] Y. Ito, S. Kuehner, S. Ghose, Phase transitions in leucite determined by high temperature, single crystal X-ray diffraction. *Zeits. Krist.* 197 (1991) 75-84. <https://doi.org/10.1524/zkri.1991.197.1-2.75>
- [28] D.C. Palmer, M.T. Dove, R.M. Ibberson, B.M. Powell, Structural behavior, crystal chemistry, and phase transitions in substituted leucite: High-resolution neutron powder diffraction studies, *Amer. Mineral.* 82 (1997) 16-29.
- [29] R.A. Lange, I.S.E. Carmichael, J.F. Stebbins, Phase transitions in leucite (KAlSi₂O₆), orthorhombic KAlSiO₄, and their iron analogues (KFeSi₂O₆, KFeSiO₄). *Amer. Mineral.*, 71, (1986) 937-945.
- [30] D.C. Palmer, E.K.H. Salje, W.W. Schmahl, Phase transitions in leucite: X-ray diffraction studies, *Phys. Chem. Minerals* 16 (1989) 714-719.
- [31] D.C. Palmer, Volume anomaly and the impure ferroelastic phase transition in leucite. Chapter 21 *in* E.K.H. Salje: *Phase Transitions in Ferroelastic and Co-elastic Crystals* 350-366, (1990) Cambridge University Press, Cambridge, New York.
- [32] P.J. Heaney, D.R. Veblen, A high-temperature study of the high-low leucite phase transition using the transmission electron microscope. *Amer. Mineral.* 75 (1990) 464-476.
- [33] J. Wyart, Etude sur la leucite. *Bull. Soc. France Mineral.* 61 (1938) 228-238.
- [34] G.T. Faust, Phase transition in synthetic and natural leucite. *Schweiz. Mineral. Petrogr. Mitt.* 43 (1963) 165-195.
- [35] M.A. Carpenter, E.K.H. Salje, A. Graeme-Barber, Spontaneous strain as a determinant of thermodynamic properties for phase transitions in minerals. *Eur. J. Mineral.* 10 (1998) 621-691.
- [36] D.C. Palmer, A. Putnis, E.K.H. Salje, Twinning in tetragonal leucite. *Phys. Chem. Minerals*, 16 (1988) 298-303.
- [37] S.A.T. Redfern, C.M.B. Henderson, Monoclinic-orthorhombic phase transition in the K₂MgSi₅O₁₂ leucite analog. *Amer. Mineral.* 81 (1996) 369-374.
- [38] A.M.T. Bell, C.M.B. Henderson, High-temperature synchrotron X-ray powder diffraction study of Cs₂XSi₅O₁₂ (X = Cd, Cu, Zn) leucites. *Mineral. Mag.*, 76, (2012) 1257-1280.
[doi:10.1180/minmag.2012.076.5.12](https://doi.org/10.1180/minmag.2012.076.5.12)
- [39] G.D. Gatta, N. Rotiroti, T. Boffa Ballaran, A. Pavese, Leucite at high pressure: Elastic behavior, phase stability, and petrological implications. *Amer. Mineral.* 93 (2008) 1588-1596.
<https://doi.org/10.2138/am.2008.2932>
- [40] G.D. Gatta, N. Rotiroti, T. Boffa Ballaran, C. Sanchez-Valle, A. Pavese, Elastic behaviour and phase stability of pollucite: a potential host for nuclear waste. *Amer. Mineral.*, 94 (2009) 1137-1143.
<https://doi.org/10.2138/am.2009.3195>
- [41] K.S. Knight, C.M.B. Henderson, Defining an aristotype crystal structure and crystallographic distortion in leucite/pollucite structured phases with space group $Ia\bar{3}d$. *Phys. Chem. Minerals*, 46 (2019) 595-605.
<https://doi.org/10.1007/s00269-019-01025-1>
- [42] Powder Diffraction File. <http://www.icdd.com/>

- [43] R. Klaska, Ein synthetischer Leucit-typ mit Ordnungstendenz. *Naturwissenschaften* 65 (1978) 592-595
- [44] H.M. Rietveld, A profile refinement method for nuclear and magnetic structures. *J. Appl. Cryst.* 2 (1969) 65-71. <https://doi.org/10.1107/S0021889869006558>
- [45] J. Rodriguez-Carvajal, Recent advances in magnetic structure determination by neutron powder diffraction. *Phys. B: Condens. Matter* 192 (1993) 55-69. [https://doi.org/10.1016/0921-4526\(93\)90108-1](https://doi.org/10.1016/0921-4526(93)90108-1)
- [46] J. Barbier, M.E. Fleet, Investigation of structural states in the series $\text{M}\text{GaSi}_2\text{O}_6$, MAlSi_2O_6 , $\text{M}\text{GaGe}_2\text{O}_6$ ($\text{M} = \text{Na}, \text{K}$). *J. Solid State Chem.*, 71 (1987) 361-370. [https://doi.org/10.1016/0022-4596\(87\)90243-X](https://doi.org/10.1016/0022-4596(87)90243-X)
- [47] R.D. Shannon, Revised effective ionic radii and systematic studies of interatomic distances in halides and chalcogenides. *Acta Cryst. A* 32 (1976) 751-767. <https://doi.org/10.1107/S0567739476001551>
- [48] C.M.B. Henderson, D. Taylor, The structural behaviour of the nepheline family: (1) Sr and Ba aluminates (MAl_2O_4). *Mineral. Mag.* 45 (1982) 111-127.
- [49] K. Momma, F. Izumi, VESTA 3 for three dimensional visualization of crystal, volumetric and morphology data. *J. Appl. Cryst.* 44 (2011) 1272-1276. <https://doi.org/10.1107/S0021889811038970>
- [50] D.C. Palmer, E.K.H. Salje, Phase transitions in leucite: Dielectric properties and transition mechanism. *Phys. Chem. Minerals* 17 (1990) 444-452.
- [51] R.L. Jones, M. Thrall, C.M.B. Henderson, Complex impedance spectroscopy and ionic transport properties of a natural leucite, $\text{K}_{0.90}\text{Na}_{0.08}[\text{Al}_{0.98}\text{Si}_{2.02}]\text{O}_6$, as a function of temperature and pressure. *Mineral. Mag.* 74, (2010) 507-519. doi:10.1180/minmag.2010.074.3.507
- [52] H. Xu, A. Navrotsky, M.L. Balmer, Y. Su, Crystal chemistry and phase transitions in substituted pollucites along the $\text{CsAlSi}_2\text{O}_6 - \text{CaTiSi}_2\text{O}_{6.5}$ join: A powder synchrotron X-ray diffractometry study, *J. Amer. Ceram. Soc.* 85 (2002) 1235-1242. <https://10.1111/j.1151-2916.2002.tb00251.x>
- [53] R. Sadanaga, T. Ozawa, Thermal transition of leucite. *Mineral. J.* 5 (1968) 321-333. <https://doi.org/10.2465/minerj1953.5.321>
- [54] A.J. Leadbetter, A.F. Wright, The α - β transition in cristobalite phases of SiO_2 and AlPO_4 I. X-ray studies. *Phil. Mag.* 33 (1976) 105-112. DOI: 10.1080/14786437608221095
- [55] G.M. Wolten, Diffusionless phase transformations in zirconia and hafnia, *J. Amer. Ceram. Soc.* 46 (1963) 418-422. <https://doi.org/10.1111/j.1151-2916.1963.tb11768.x>
- [56] C.M.B. Henderson, The tetragonal-cubic inversion in leucite solid solutions. *Progress in Experimental Petrology*, 5th Report, Natural Environment Research Council, Series D 18 (1981) 50-54.
- [57] D.L. Hamilton, C.M.B. Henderson, The preparation of silicate compositions by a gelling method. *Mineral. Mag.* 36 (1968) 832-838.
- [58] I.S.E. Carmichael, The mineralogy and petrology of the volcanic rocks from the Leucite Hills, Wyoming. *Contr. Min. Petr.* 15 (1967) 24-66.
- [59] W.S. MacKenzie, D.M. Richardson, B.J. Wood, Solid solution of SiO_2 in leucite. *Bull. Soc. Mineral. Crist.* 97 (1974) 257-260.

- [60] B. Fultz, *Phase Transitions in Materials*. Cambridge University Press, Cambridge (2014) xxiv + 563pp.
- [61] D.E. Damby, E.W. Llewelin, C.J. Horwell, B.J. Williamson, J. Najorka, G. Cressey, M. Carpenter, The α - β transition in volcanic cristobalite. *J. Appl. Cryst.*, 47, (2014) 1205-1215.
<https://doi.org/10.1107/S160057671401070X>
- [62] P. Scherrer, Bestimmung der grösse und der inneren struktur von colloidteilchen mittels Röntgenstrahlen. *Nachr. Ges. Wiss. Göttingen* 26 (1918) 98–100.
- [63] A. L. Patterson, The Scherrer Formula for X-Ray Particle Size Determination. *Physical Review* 56 (1939) 978-982. <https://doi.org/10.1103/PhysRev.56.978>
- [64] R.H. Mitchell, S.C. Bergman, *Petrology of Lamproites*, 6.6.1, Plenum Press, New York, 1991.
- [65] F. Frey, H. Boysen, T. Vogt, Neutron powder investigation of the monoclinic to tetragonal phase transformation to undoped zirconia. *Acta Cryst. B*46 (1990) 724-730.
<https://doi.org/10.1107/S010876819100856X>
- [66] E.K.H. Salje, *Phase transitions in ferroelastic and co-elastic crystals*. Cambridge University Press, Cambridge, New York, (1990) xiii + 366 pp. + 53 pp. app.
- [67] E.K.H. Salje, Domain boundary engineering. *Phase Transitions* 82 (2009) 352-469.
<https://doi.org/10.1080/01411590902936138>